ADSORPTION OF Cr AND Fe IONS ON BEYPAZARI LIGNITE AND THEIR EFFECT ON DECARBOXYLATION

M.Akgül , A.Karabakan
Department of Chemistry, Hacettepe University,
Beytepe, 06532 Ankara, Turkey

Y.Yürüm
Faculty of Engineering and Natural Sciences, Sabanci University,
Tuzla, 81474 Istanbul, Turkey

Introduction

The presence of copper catalyzed decarboxylation reactions of lignites.[1,2] Starting at around 160°C, however, the catalytic effect of copper becomes significant and an increase of the order of 20% is observed in the higher heating value of the heat-treated lignite. Increasing the concentration of copper to values greater than 1% appears to have essentially no effect on its catalytic activity. The purpose of the present study is to investigate the effects of the transition metal ions Fe^{3+} and Cr^{3+} , loaded onto the lignite, on the decarboxylation of Beypazari lignite, in terms of energies of activation for the decarboxylation processes, the calorific values, the burning profile peak temperatures of the lignite samples obtained as a result of the decarboxylation process.

Experimental

Turkish Beypazari lignite (61.2% C) sample was ground to –65 mesh ASTM under nitrogen atmosphere, dried to constant weight at 110°C under vacuum and stored under nitrogen atmosphere. Pore volumes and average pore diameter greater than 20A o were determined by mercury porosimeter up to 2000 kg / cm 2 using a Carlo Erba model 200. The surface area of the coal sample was measured with a surface area apparatus (BET method). The lignite sample was demineralized with standart methods. Lignite samples about 5 g were stirred for 24 hours with solutions of chloride salts of Cr^{3+} and Fe^{3+} ions under the nitrogen atmosphere. Metal loading experiments were carried out for the wt% metal loadings of about 1, 2, 3, 4, 5% of the d.a.f. coal sample. The metal loaded lignite samples were decarboxylated at 100, 150, 200 and 230°C for a period of 30 minutes. For comparison purposes, blank samples of original and demineralized coal (i.e. containing no metal) subjected to exactly the same procedure, except that the initial slurry was made with distilled water. Calorific values of all lignite samples were determined. The sample which has the highest calorific value was determined in each lignite group. The selected coal samples (metalloaded), the blank original and demineralized coal samples were decarboxylated at 100, 150 and 200 °C for the periods of 10, 20, 30, 40, 50 and 60 minutes in the vacuum oven under nitrogen atmosphere. Then, by using the DSC device, coal samples obtained from the decarboxylation experiments were oxidized for 10 and 60 minutes starting from 35°C upto 500°C. Kinetics of the decarboxylation reactions was investigated for the blank original (no metal loading), the blank demineralized (no metal loading) and the selected samples that have optimum calorific value from each group. FTIR spectra of original (blank and metal loaded) and demineralized (blank and metal loaded) lignite samples were measured with a Mattson 1000 FTIR spectrometer.

Results and Discussion

The pore radii of Beypazari lignite were found to change between 10 and 40 nm. This indicates that the lignite contains mainly mesopores.

Decarboxylation process has been shown to increase the calorific value of low-rank coals. The calorific value of the original and demineralized Beypazari lignite was measured as 3663.4 J/g and 7435.7 J/g, respectively. In order to determine the experimental conditions for the most efficient results in terms of the highest calorific value of the lignite with plausible wt% metal loading and decarboxylation temperature after metal treatment, a set of experiments was carried out.

The decarboxylation experiments were carried out with the samples that have the wt% metal loading values between 1-5 % and decarboxylation temperature values of 100°C, 150°C, 200°C and 230°C. The duration of the decarboxylation experiments was kept constant at 30 minutes. To determine the optimum values of wt% metal loading and decarboxylation temperature for the best efficiency of metal catalyst, the calorific values of the samples were measured. The results obtained for the Fe^{3+} loaded original lignite show that; i) The variation of calorific value with wt% metal loading appears to pass through a maximum at 2% metal loading and then decrease with increasing wt% metal loading. ii) The variation of calorific value with decarboxylation temperature appears to pass through a maximum at 150°C and then decrease with increasing temperature. Also, it is apparent that the calorific values of the metal loaded original coal samples are greater than those of the blank original coal samples at all decarboxylation temperatures. The results obtained for the Cr^{3+} loaded original lignite show that; i) The variation of calorific value with wt% metal loading appears to pass through a maximum at 2% metal loading and then decrease with increasing wt% metal loading . ii) The variation of calorific value with decarboxylation temperature appears to pass through a maximum at 150°C and then decrease with increasing temperature. Also, it is apparent that the calorific values of the metal loaded original coal samples are greater than those of the blank original coal samples at all decarboxylation temperatures.

The results obtained for the Fe^{3+} loaded demineralized lignite show that; i) The variation of calorific value with wt% metal loading appears to pass through a maximum at 1% metal loading and then decrease with increasing wt% metal loading . ii) The variation of calorific value with decarboxylation temperature appears to pass through a maximum at 150°C and then decrease with increasing temperature. Also, it is apparent that the calorific values of the metal loaded demineralized coal samples are greater than those of the blank original coal samples at all decarboxylation temperatures.

The results obtained for the Cr^{3+} loaded demineralized lignite show that; i) The variation of calorific value with wt% metal loading appears to pass through a maximum at 1% metal loading and then decrease with increasing wt% metal loading .ii) The variation of calorific value with decarboxylation temperature appears to pass through a maximum at 150°C and then decrease with increasing temperature. Also, it is apparent that the calorific values of the metal loaded original coal samples are greater than those of the blank original coal samples at all decarboxylation temperatures.

After the determination of the calorific values, it is seen that the calorific values of the decarboxylated Beyapazari lignite samples with catalyst (that is metal loaded) are higher than those of the blank (no metal loading) lignite samples. As the decarboxylation temperature was increased calorific value of the lignite also increased reaching to a maximum value at 150°C and further increase in the temperature caused a decrease in the calorific value of the lignite. In all of the experiments the measured calorific values of the metal loaded and decarboxylated lignite samples were higher than those of the blank (no metal loading) and undecarboxylated lignite samples. The optimum wt% metal loading and reaction temperature in the decarboxylation experiments to obtain decarboxylated lignites with

the highest calorific value for each group of the metal loaded lignite samples are given below:

For original lignite samples:
Fe 2% – 150°C, Cr 2% – 150°C
For demineralized lignite samples:
Fe 1% – 150°C, Cr 1% – 150°C

Kinetics of The Decarboxylation Reaction. To evaluate the data, first order reaction kinetics were assumed for decarboxylation reactions of lignite samples. Metal ions acted as catalyst.

Table 1. The Activation Energies of the Decarboxylation Reactions of Metal Loaded Original and Demineralized Lignite Samples

Coal Sample	Activation Energy (kj/mol)
Original coal	69.9
Demineralized coal	60.7
Cr^{3+} loaded original coal	37.8
Fe^{3+} loaded original coal	39.8
Cr^{3+} loaded demineralized coal	39.6
Fe^{3+} loaded demineralized coal	41.9

After the computation of the energy of activation for the decarboxylation of each type of coal samples, it is apparent that the activation energy values for the metal loaded coal samples are lower than the energy of activation values for the decarboxylation of the blank (no metal loaded) original and demineralized coal samples. This results are consistent with the idea that the metal ions loaded on coal behave as a catalyst in coal processing, like the decarboxylation of coal.

References

(1) Stournas, S.; Papachristos, M.; Kyriacopoules, G.B.. *Fuel Processing Technology*, **1987**, *17*, 195.
(2) Özvatan, S.; and Yürüm, Y. *Energy Source*s, **2000**, in press.

Aggregation and Adsorption of Asphaltenes: A kinetic Study.

Sócrates Acevedo[a,*], María A. Ranaudo[a], Coromoto García[a], Jimmy Castillo[b], Alberto Fernández[b, *]. [a]Laboratorio de Fisicoquímica de Hidrocarburos, [b]Laboratorio de Espectroscopia Laser. Universidad Central de Venezuela, Facultad de Ciencias, Escuela de Química, 47102, Caracas 1041, Venezuela

Introduction

Adsorption kinetics could be a useful and simple tool for the study of asphaltene aggregation in solution and some preliminary results has been reported[1]. In principle adsorption of aggregates should lead to different adsorption rate constant k depending on aggregate size. Since a dependence of aggregate size with concentration could be expected this should lead to a dependence of k and ν_∞ with concentration. Here ν_∞ is the surface concentration ν required for surface saturation (see below). It has been reported elsewhere[1] that for diluted toluene solutions, adsorption of asphaltenes on silica is an essentially irreversible process. As shown below this fact could be used to simplify the adsorption kinetics. In this paper, we have measured the adsorption kinetics of several asphaltenes solutions at the silica – toluene interface. The results were fitted to a second order irreversible kinetics and the k and ν_∞ evaluated. As shown below, the strong dependence of these parameters on initial C_0 concentration could be allow for in terms of aggregate size in solution.

Experimental

Asphaltenes were obtained from Furrial oil (20° API) by addition of 40 volumes of n – heptane. The flocculated solid was thoroughly washed with this solvent in Soxhlet as described earlier[2]. A thin layer silica gel 60 supported on Teflon plates, (from Merck) was used. Kinetic measurements were performed by dipping the plates within vials containing the toluene solutions of asphaltenes (5 to 3000 mg/L). Absorbance changes with time was monitored using a He – Ne laser beam (632.8 nm) by passing the beam through solution and solvent using a beam splitter.

Kinetics plots wereobtained by plotting the solution absorbance $A(t)$ as function of the time. $A(t)$ was converted to solution concentration $C_S(t)$ (mg/L) using equation 1:

$$C_S(t) = A(t)\frac{C_0}{A_0} \qquad 1$$

Here C_0 and A_0 are the initial concentration and initial absorbance respectively. Amount adsorbed at any time ν (mg L^{-1}) was obtained from equation 2 and could be converted to mg/g using equation 3.

$$\nu = C_0 - C_S(t) \qquad 2$$

$$\nu = [C_0 - C_S(t)]\frac{V}{m} \qquad 3$$

Here V is the solution volume (L) and m the mass of silica (g).

Kinetic runs were fitted to a second order Langmuir type irreversible process. The corresponding equation was derived as follows. Let ν be the amount of sample adsorbed after time t. Let C_0 be the initial solution concentration. Let k and ν_∞ be the second order rate constant and the saturating surface concentration respectively. Then the increase of ν with time can be written as follows:

$$\frac{d\nu}{dt} = k(\nu_\infty - \nu)(C_0 - \nu) \qquad 4$$

Solution of this equation is:

$$\nu = C_0\nu_\infty \frac{\exp[(C_0 - \nu_\infty)kt] - 1}{\exp[(C_0 - \nu_\infty)kt]C_0 - \nu_\infty} \qquad 5$$

It could be easily shown that for any values of C_0, ν_∞ and k, ν will increase from 0 to the limiting value of ν_∞ when either the time or C_0 are increased.

Results and Discussion

Figure 1 shows the results of the kinetic run for C_0 = 200 mgL^{-1}. Similar results were obtained for other initial concentrations and the complete results are shown in Table 1. In this Figure, the points are experimental and the curve is the fitting to equation 5 with the corresponding k and ν_∞ values. As shown in Table 1, these parameters depends strongly on C_0. Thus over the concentration range, k decreases 760 fold whereas ν_∞ increases about 100 fold.

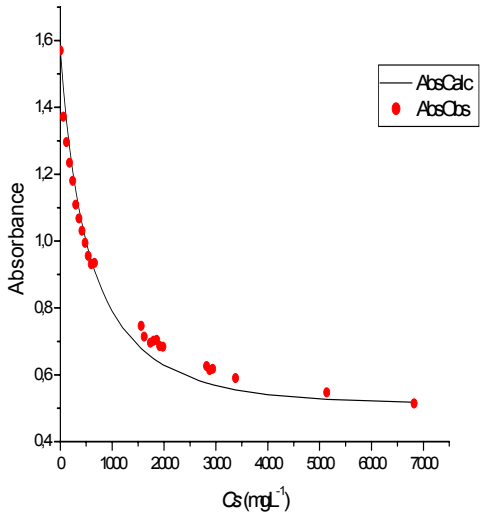

Figure 1. Comparison of observed and calculated absorbances for C_0 = 200 mgL^{-1}. Curve is the fitting of equation 5 to the experimental results.

Table 1. Change of Second Order Rate Constant k and v_∞ With the Initial Concentration C_0

C_0 (mg L^{-1})	v_∞ (mg g^{-1})	k (L s^{-1} mg^{-1})	k/k_5
5	1.58	3.8E-4	1
20	4.32	1.0E-4	3.8
50	13.61	5E-5	7.6
100	10.88	4E-5	9.5
200	43.04	1E-5	38
400	118.7	2.7E-6	140
800	103.7	1.00E-6	380
1500	160	8.00E-7	475
3000	160	5.00E-7	760

These results are consistent with aggregate formation in solution and with a change in aggregate size as the initial concentration is increased. A decrease in k should be expected with an increase in aggregate size. This could easily be seen using a simple mass balance argument. Let A_T be the total molar concentration of asphaltene (equivalent to C_0), let A_S be the molar solution concentration of free asphaltene (equivalent to C_S) and let A_n be the molar concentration of aggregates where n is aggregation number. Then according to mass balance:

$$A_T = A_S + n\ A_n \qquad 6$$

Adsorption on the silica surface occurs through bonding between functional groups in molecules and sites on the silica surface. Let f_i be the number of these functional groups in each molecule. Their total number in solution would be:

$$A_T\ f_i = A_S\ f_i + n\ (f_i\ A_n) \qquad 7$$

As suggested by equation 7, many functional groups would be involved in aggregate formation and would not be available for adsorption. In other words, all but those in the aggregate surface would not be available for adsorption.

Figure 2 is a plot of –ln k against C_0 which suggest that aggregate size grows "sigmoidaly" with C_0, approaching a sort of limiting size.

One could imagine that, when contacted with the silica surface, every solution in Table 1 "sees" the same surface. Thus the high values of v_∞ found at most C_0 in Table 1 should be due mainly to aggregate adsorption and not to multilayer formation. In principle mean aggregate size could be estimated from these v_∞ values.

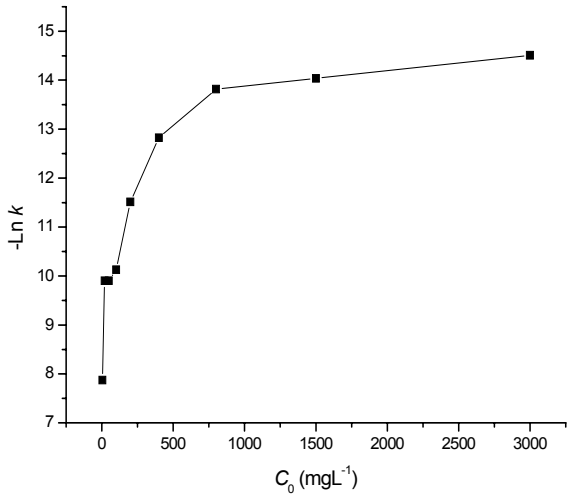

Figure 2. Change of –Ln k with the initial concentration C_o

Acknowledgements

The financial support of FONACIT (Grants G97000722 and 97004022) and CDCH (Grants 03124897/98, 03123872/98, 03124031/97) is gratefully acknowledged. We also thank the technical support of Lic. Betilde Segovia and Mr. Juvenal Ochoa.

References

1. Acevedo, S; Ranaudo, M. A. García, ;C. ; Castillo, J; Fernández, A.; Caetano, M.; Goncalvez, S.; *Colloids and Surfaces* A, **2000**, *166*, 145 – 142.
2. Gutierrez, L. B.; Ranaudo, M.A..; Méndez, B.; Acevedo, S. *Energy & Fuels*, **2001**,*15* 624 - 628.

Application of Group Contribution Method in Predicting V-L Equilibrium of ShengLi Heavy oil

Yanmei Zhang Conggang Wang

State Key Laboratory of Heavy Oil Processing
Department of Chemical Engineering, University of Petroleum,
Dongying, Shandong, 257061, P.R. China

Preface

Group contribution methods have been used to calculate the properties of pure components, such as viscosity, surface tension, critical property etc.。Recently，group contribution methods are also used to predict vapor liquid equilibrium of the systems in which the composition of the components can be known exactly.

In this paper, the group contribution method is used to predict the vapor liquid equilibrium of the heavy oil which is a complex mixture.

Experiment

With the flow equilibrium unit, the V-L equilibrium data were obtained. The experiments were done under two different pressures and five different temperatures. At the same time, the feed was cut by TBP instrument into narrow fractions of which the properties were measured.

Group Contribution Method

Assume that the narrow fractions can be thought as pseudo-components, thus petroleum is considered as a mixture of these components. Then the V-L equilibrium relation can be treated as that of the mixture.

With the given flow and composition of the feedstock, under a certain pressure, if flashing temperature is defined, the vaporization ratio can be calculated and if the vaporization ratio is defined the flashing temperature can be calculated.

The application of group contribution method in predicting V-L equilibrium of petroleum requires that the group compositions of petroleum must be determined. The methods such as Model Compounds method，n-d-M-LP method and Model Molecule method are available. Although these methods are effective to a certain extent in the predicting of V-L equilibrium, they need much more properties and the process is complex. In this paper, normal paraffin model molecule method is used to determine the group composition and the procedure is

Cut the oil into narrow fractions with TBP data;

Assume that every narrow fraction consists of normal paraffin which has the same properties as the fraction's;

The number of group - CH_3 in each model molecule always equals 2, and that of - CH_2 -group can be any positive number.

Then the group composition can be determined by the molecular weight or the boiling point of the narrow fraction.

In general, under atmospheric and vacuum conditions, the V-L equilibrium constants K can be calculated as follow,

$$K_i = \frac{\gamma_i P_i^s}{P} \tag{1}$$

In the equation, P_i^s is the saturated vapor pressure of component i under the system temperature, γ_i is the activity coefficient of component i in the liquid phase，P is the system pressure. P_i^s is calculated by the method for predicting saturated vapor pressure of pure compounds proposed by Jensen. γ_i is calculated using modified UNIFAC(Larsen and Kikic) method.

Saturated Vapor Pressure Model of Group Contribution—Jensen Model

$$RT\ln(\phi_i^s P_i^s) = \sum \nu_k^{(i)} \Delta g_k + RT\sum \nu_k^{(i)} \ln \Gamma_k^{(i)} \tag{2}$$

$$\sum \nu_k^{(i)} \Delta g_k = \sum \nu_k^{(i)} \Delta g_k^{'} + \Delta G_i^{'} \tag{3}$$

$$\Delta g_k^{'} = A_{k,1} / T + A_{k,2} + A_{k,3} T + A_{k,4} \ln T \tag{4}$$

$$\Delta G_i^{''} = \sum\sum \nu_{kj}^{(i)} \Delta g_{kj}^{''} \tag{5}$$

In the above relations, ϕ_i^s is the fugacity coefficient of saturated vapor of component i，and it is approximately equals 1.0.； Δg_k is the Gibbs energy function of group k，depending on the temperature and the structure of the molecule; $\Gamma_k^{(i)}$ is the activity coefficient of group k in component i ,calculated by the residue term in UNIFAC activity coefficient model； $\nu_k^{(i)}$ is the number of group k in component i ； $\nu_{kj}^{(i)}$ is the contribution number of *j* type structure in group *k* of component *i*, $A_{k,1}$ is the group parameter of group *k*。

When normal paraffin model molecule method is used to determine the group composition, there are only two types of group in pseudo components,—-CH_3 and -CH_2-, thus

$RT\sum \nu_k^{(i)} \ln \Gamma_k^{(i)} = 0$ ， $\Delta G_i^{''} = 0$ ， the method is simplified,

$$RT\ln P_i^s = \sum \nu_k^{(i)} \Delta g_k^{'} \tag{6}$$

Activity Coefficient Model

In UNIFAC activity coefficient model

γ_i is consisted of two parts γ_i^c and γ_i^R ,

$$\ln \gamma_i = \ln \gamma_i^c + \ln \gamma_i^R \tag{7}$$

For normal paraffin model molecule method $\ln \gamma_i^R = 0$, thus,

$$\ln \gamma_i = \ln \gamma_i^c \tag{8}$$

Larsen suggested that γ_i^c could be calculated with the two relations below,

$$\ln \gamma_i^c = 1 - \omega_i + \ln \omega_i \tag{9}$$

$$\omega_i = r_i^{2/3} / \sum_j x_j r_j^{2/3} \tag{10}$$

Kikic suggested that γ_i^c could be calculated with another two relations ,

$$\ln \gamma_i^c = \ln \frac{\omega_i}{x_i} + 1 - \frac{\omega_i}{x_i} - 5q_i(1 + \ln \frac{\Phi_i}{\theta_i} - \frac{\Phi_i}{\theta_i}) \tag{11}$$

$$\omega_i = r_i^{2/3} / \sum_j x_j r_j^{2/3} \quad (12)$$

Predicting Results

By the above method, calculation of flashing temperature and vaporization ratio was made for ShengLi heavy oil and the results are shown in table 1 and table 2.

Table 1 Deviations of flashing temperature predicted by group contribution methods

Model	Kikic	Larsen
AAD，ΔT,K	11.47	11.54
ARD，(%)	1.92	1.93

Table 2 Deviations of flashing vaporization ratio predicted by group contribution methods

Model	Kikic	Larsen
AAD，ΔE,%	4.00	4.02
ARD，(%)	23.62	23.81

$$\text{AAD}=\frac{1}{N}\Sigma\left|calculated-\exp erimental\right|$$

$$\text{ARD}=\frac{1}{N}\Sigma\left[\left|\frac{calculated-\exp erimental}{\exp erimental}\right|\right]\times 100\,\%$$

The results in the above tables are not satisfactory and so the model parameter are to be modified.

Modification of the Parameter in Jensen Model and the Predicting Results

The parameters provided by the vapor pressure model are obtained from the Antoine equation，and the data involving that of C_3 to C_{18}. However, for Shengli heavy oil, the carbon numbers of the fractions are from 22 to 76, far beyond the application range. Therefore twelve normal hydrocarbons whose carbon numbers are from 22 to 76 are chosen to get the new parameters. The data involve 72 points which are obtained under different experimental temperatures. The modified parameters are shown in table 3. With Larsen and Kikic model, the flashing temperatures and vaporization ratios are predicted and the results are shown in table 4.

Table 3 Modified parameters of Jensen model

Item	Parameters for $-CH_3$	Parameters for $-CH_2-$
$A_{k,1}$	2.03122×10^4	9.03611×10^4
$A_{k,2}$	-8.49432×10^3	-7.11573×10^3
$A_{k,3}$	2.21895	-0.788164
$A_{k,4}$	1.55162×10^3	1.11290×10^3

Table 4 Deviation of predicting results with modified parameters

Item	Flashing temperature		vaporization ratio	
	Kikic K	Larsen K	Kikic K	Larsen K
AAD	4.72	4.74	1.49	1.50
ARD,%	0.79	0.79	7.69	7.77

From the data in table 4，It can be found that with the modified parameter，the AAD and ARD of predicted temperatures by Kikic model are reduced from 11.47K and 1.92% to 4.72K and 0.79% respectively；and that of predicted vaporization ratios are reduced from 4.00% and 23.62% to 1.49% and 7.69% respectively. The AAD and ARD of predicted temperatures by Larsen model are reduced from 11.54K and 1.93% to 4.74K and 0.79%；and that of predicted vaporization ratios are reduced from 4.02% and 23.81% to 1.50% and 7.77% respectively. The deviations are descended obviously, i.e., the accuracy is enhanced greatly.

Conclusion

With the normal paraffin model molecule to determine the group composition, Larsen and Kikic group contribution models for γ_i were used to predict the V-L equilibrium of ShengLi reduced crude. It was found that the results were not satisfactory. By modifying the parameter in the vapor pressure model, the results of flashing temperatures and vaporization ratios match the experimental data satisfactorily. The AAD and ARD of predicted temperatures by Kikic model are 4.72K and 0.79% respectively； and that of predicted vaporization ratios are 1.49% and 7.69% respectively. The AAD and ARD of predicted temperatures by Larsen model are 4.74K and 0.79%；and that of predicted vaporization ratios are 1.50% and 7.77% respectively.

Reference

(1) Jensen,J.G, Frendenslund Aa and Rasmussen, P., *I&EC*, 1982,22(1),49

(2) Frendenslund ,Aa and Praunitz,J.M ,*AICHE J.* ,1975,21,1086

(3) Kikic I. and Frendenslund Aa, *The Canadian Journal of Chemical Engineering*, 1980, 58,4

(4). Larsen B. L. et al., *Ind. eng. Chem. Res*. 1987,26(11),2274

Delete this page

The effect of local charge on coal reactivity modeled with a single large polymer macromolecule.

Erik Kroo

Hydrocarbons Group, Advanced Fuel Research Inc.

87 Church Street, East-Hartford, CT 06108-3742)

Introduction

Coal is thought of as a network of macromolecules or matrix of clusters consisting mainly of crosslinked polymers where the average monomer units are built predominantly from aromatic rings connected with aliphatic bridges. This concept has gained acceptance, because it could be applied to a vide range of phenomena of coal chemistry. Difficulties arise when contributions from weak interactions are entering the picture. Weak interactions have been recognized as important but contributions like hydrogen bonding (1) or associative forces (2) to coal crosslinking and coal structure in general is not clear. Recently first principle modeling efforts in complex systems have significantly increased and this has precipitated to the field of coal chemistry too. For example simulation of solvent swelling (3) or molecular associations (4) have addressed the role of weak interactions in coal. However, first principal methods are presently limited by the size of complex networks like coal. On the other hand, semiempirical methods, which can handle larger sized systems, are limited by the approximations in the computational methods themselves. If coal is treated as a single molecule, the strong and intermediate interactions can be lumped together. This concept holds the promise for a more general coal reactivity model if a suitable description, for example density functional representation, can be found. It will be shown in this paper that, using several simple approximations and the concept of coal as a large polymer macromolecule, a variety of product yields in low rank demineralized and ion exchanged coals can be predicted.

Experimental

Part of the data used in this study was published earlier (5). Zap lignite and Wyodak subbituminous (Argonne Nat.Lab Coal Bank) coals were demineralized and ion exchanged at pH 8 with Ca^{++}, Ba^{++} and K^{+}. Demineralization, ion exchange and remoisturization of the samples were carried out in nitrogen atmosphere and the technique was described in an earlier publication (5).

Table 1.Amount of cations exchanged into demineralized coals.

	daf% grmol./100gr	
	Zap	Wy.
Ca^{++}	0.94	0.87
Ba^{++}	1.31	1.08
K^{+}	2.07	1.61

The amount of the ion exchanged cations were determined from the ash content of the demineralized ion exchanged samples (CaO; BaO;K_2O) and the results are shown in Table 1. The ash content, water evolution and pyrolytic tar formation was measured using a Thermo-Gravimetric Furier-Tansform Infrared (TG-FTIR) method (6). Only particular products that are formed in quasi isoenergetic processes will be studied in this paper. This is approximately true for large molecules like tar and asphaltenes where secondary processes average out. However this is not true for water. Therefore the water yields were curve resolved as shown in the example of a demineralized Zap lignite sample (Fig.1.)

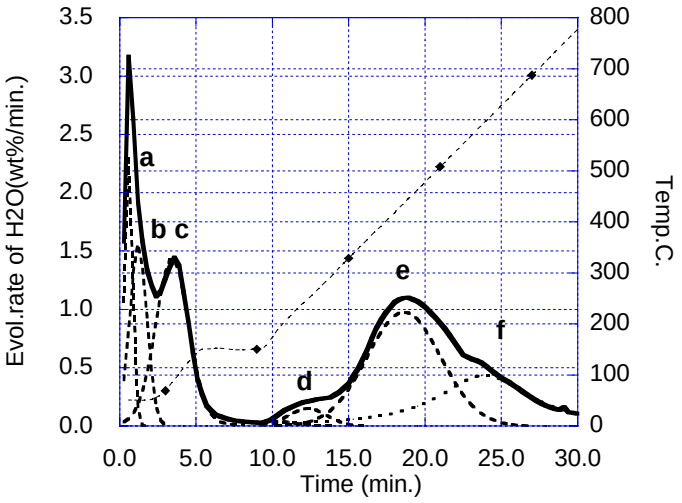

Figure 1. TG-FTIR water evolution of demineralized Zap lignite, curveresolved into six (a-f) individual water evolution peaks.

Typically there is a very fast water loss at the beginning of the measurement, which cannot be picked up by the instrument. Therefore the first peak (peak a in wet coal, peak b in dry coal) was determined from the weight loss measured by the balance below 140C^{o} Sum=weight$_{init}$-weight$_{140C}$ and a(wet)=Sum-b-c as well as b(dry)=Sum-c. In dry coals peak a disappears. The higher temperature d, e and f peaks are formed in secondary processes, therefore only the first three peaks were used.

The liquefaction was carried out in a bomb reactor at 400C^{o} for 30 minutes in tetraline. For more details of the liquefaction technique see (7).

Discussion

The formation of a particular primary product, P as a fragment (water, tar, asphaltene) of the initial coal molecule is simply

$$C_{(i)} \rightarrow C_{(r)} + P \qquad (1)$$

where $C_{(i)}$ and $C_{(r)}$ are the initial and resultant coal molecule. If the macromolecule is sufficiently long and consists of repeat units so that, similar to depolymerization, every fragmentation occurs at similar chemical sites, the product formation after m fragmentation is

$$C_{(A)} \rightarrow C_{(B)} + mP \qquad (2)$$

and the reaction is driven by the energy difference between $C_{(A)}$ and $C_{(B)}$ such that

$$\Delta E = E[C_{(A)}] - E[C_{(B)}] = \chi\, m \qquad (3)$$

In real processes m is large, in which case eq.2-3 does not require a rigorous distribution of identical fragmentation sites but rather a statistical one with the only remaining condition, that the formation of the particular product is isoenergetic..

According to the "density functional theory" (8) the ground state of a multielectron system is completely determined by the

electron density function $n(r^{\rightarrow})$ and the physical quantities of interest (energy, quantum state, etc.) can be expressed as functionals of $n(r^{\rightarrow})$. The advantage of this treatment is that one can take out trivial terms of interaction. For example in the presence of an external potential, $\varphi(r^{\rightarrow})$, the energy is

$$E = \int \varphi(r^{\rightarrow}) n(r^{\rightarrow}) d^3 r^{\rightarrow} + G[n(r^{\rightarrow})] \quad (4)$$

where the functional $G[n(\varphi(r^{\rightarrow})]$ gathers the contributions from exchange, correlation, coulombic and kinetic energy. If the external potential is replaced by a uniform distribution of local potentials U, the energy is simply

$$E \approx NU[n'(r^{\rightarrow})] + G[n(r^{\rightarrow})] \quad (5)$$

where $n'(r^{\rightarrow})$ is a local electron density function and N is the number of the local potential sites. Than the yield of a particular product

$$m = \frac{\Delta E}{\chi} \approx NU[n'_{(A)}(r^{\rightarrow}) - n'_{(B)}(r^{\rightarrow})] + \\ + \{G_{(A)}[n_{(A)}(r^{\rightarrow})] - G_{(B)}[n_{(B)}(r^{\rightarrow})]\} = \\ A' + B'(NU) \quad (6)$$

Consequently, if the single molecule concept is applicable, particular product yields can be evaluated as linear functions of nU.

It was expected that an appropriate distribution of local potentials in coal can be established with ion exchange of cations into demineralized coal. Demineralization is necessary to avoid interactions with mineral matter. Than the remaining task is to calculate U from the electrostatic potential of cations, and test the validity of eq.6. through linear fitting with a number of cations.

U was calculated in the following simple model:

a. The medium around the cations is divided in two continuous phases separated by a sharp boundary, and the cations are situated at the boundary.
b. The cations are represented as charged spheres characterized by the electrostatic potential at a distance, a, from the center (r = a) where a is the ionic radius. This potential will be taken as the sum of a direct and an image potential. The usually small exchange and correlation factors will be neglected. The image potential is compensating for the field line bending at the boundary.
c. If there are mobile charges present at the boundary, this will have a screening effect on the local field. Therefore the local potential will be calculated separately in the presence and absence of mobile charges.

The electric field of a charged sphere equals the surface charge divided by the permittivity of the medium (κ: dielectric constant, ε_0: vacuum permittivity) in what we will call the direct potential

$$u_{(dir.)}(r = a) = \frac{Q}{4\pi\kappa\varepsilon_0 a^2} = Const.\frac{Q}{a^2} \quad (7)$$

If mobile charges are present (9), the direct potential is

$$u_{(dir)}(r = a) = \frac{Q}{4\pi\kappa\varepsilon_0 r}\left[\frac{\lambda_D}{\lambda_D + a}\right]\exp\left[-\frac{r-a}{\lambda_D}\right] \quad (8)$$

Since the Deby length $\lambda_D >> a$, eq.4 reduces to

$$u_{(dir.)}(r = a) \approx \frac{Q}{4\pi\kappa\varepsilon_0 a} = Const.\frac{Q}{a} \quad (9)$$

The correction for the image potential is

$$u_{img.}(r = a) = \frac{Q^2}{4\pi\varepsilon_0}\frac{\kappa^1 - \kappa^2}{\kappa^1 + \kappa^2}\frac{1}{4\kappa^2 a} = Const.\frac{Q^2}{a} \quad (10)$$

Than the full potential, U is the sum of the direct and image potential. It is useful to write U as the normalized sum of $u_{(dir.)}$ and $u_{(img.)}$ with the parameter $x \leq 1$

$$U = xu_{(dir.)} + (1-x)u_{(img.)} \quad (11)$$

Let the normalized yield of a particular product $m/N = m(\pi)$ in the presence and $m/N = m(\delta)$ in the absence of mobile electrons in the vicinity of cations. Substituting eq.11 into eq.6 we get

$$m(\pi) = A + B\left(x\frac{Q}{a} + (1-x)\frac{Q^2}{a}\right) \quad (12)$$

$$m(\delta) = A + B\left(x\frac{Q}{a^2} + (1-x)\frac{Q^2}{a}\right) \quad (13)$$

Consequently, the values of A, B and x can be determined from the normalized product yields obtained with a set of ion-exchanged coals.

Results

Table 2. shows the normalized (m/N) water evolution, pyrolysis tar and liquefaction asphaltene yields of demineralized and ion exchanged Zap lignite as well as subbituminous Wyodak coals. The number of cations was defined on dry ash free bases as N=mg.mol. exchanged cation./100gr coal (Table 1.). Note that, per definition, N does not change as a result of product formation. The carboxyl hydrogen concentration $[H_{carb.}]$ was calculated from the average value obtained from ion exchange with the three cations assuming, that cations exchange exclusively with the carboxyl hydrogens:

$$[H_{carb.}] = 2([Ca^{++}]+[(Ba^{++}]+[K^{+}/2])/3. \quad (14)$$

In some cases certain trends of yields with the cationic strength can be observed. For example the water, tar and asphaltene yields typically decrease with the cationic strength ($Ca^{++} \rightarrow Ba^{++} \rightarrow K^{+}$) in Zap lignite. However this is not observed with Wyodak coal (see peak a and b (wet coals), peak c (dry coals)). What is expected is, that the results of the linear data-fit calculation would provide some

insight into this and perhaps, to the differences between Zap and Wyodak

Table 2. Normalized water, tar and asphaltene yields with wet and dry demineralized and ion exchanged Zap and Wy. coals

Wet		daf% H_2O Peak			daf%	
		a	b	c	tar	asphalt.
Zap	Demin.	5.2	0.4	1.4	7.4	9.9
	Ca^{++}	13.5	6.4	3.8	11.6	11.4
	Ba^{++}	9.6	8.3	3.6	6.7	6.6
	K^{+}	5.5	0.4	2.2	4.4	1.8
Wy	Demin.	5.6	0.9	1.6	13.7	25.2
	Ca^{++}	16.3	0.6	3.1	16.9	21.7
	Ba^{++}	7.6	10.2	3.1	15.6	16.6
	K^{+}	10.3	0.4	1.0	9.5	16.3
Dry						
Zap	Demin.		0.4	1.0	9.0	11.0
	Ca^{++}		1.6	4.0	10.1	13.1
	Ba^{++}		1.1	3.2	4.4	9.1
	K^{+}		0.6	2.4	4.6	7.0
Wy	Demin.		0.6	0.6	15.1	17.7
	Ca^{++}		1.2	3.8	15.6	12.0
	Ba^{++}		1.7	2.8	13.6	11.1
	K^{+}		0.8	1.4	9.9	12.2

Table 3. Results of the linear fit calculations.

		WET COAL		DRY COAL	
		Zap.	Wy.	Zap.	Wy.
A	H_2O (a)	-1.6	5.5	—	—
	H_2O (b)	0.9	5.2	-0.4	1.1
	H_2O (c)	3.1	3.3	1	0
	tar	-7.4	11.9	-1.8	-6.6
	asph.	-6.6	2.2	-1.9	1.8
B	H_2O (a)	13.6	19.5	—	—
	H_2O (b)	-14	-31.1	1.4	-2
	H_2O (c)	4.5	-8.7	2.7	1.9
	tar	13.4	-14.6	27	4.5
	asph.	16.4	36.9	20.9	3
x	H_2O (a)	0.85	0.76	—	—
	H_2O (b)	0.60	0.69	0.90	0.66
	H_2O (c)	0.64	0.67	0.85	1.0
	tar	0.90	0.61	0.80	1.0
	asph.	0.85	0.75	0.79	0.67
Mode	H_2O (a)	**π**	**δ**	—	—
	H_2O (b)	***δ***	***δ***	**π**	**π**
	H_2O (c)	**π**	**π**	**δ**	**π**
	tar	**π**	**π**	**π**	***δ***
	asph.	**π**	**π**	**π**	***δ***

.

Fortunately in every case that was studied, a solution was found with either eq.12 (π) or eq.13. (δ), and the results are shown in Table 3. Keep in mind that **A** is related to local charge density difference, **B** is related to energy difference for the whole molecule, **x** accounts for the ratio of direct to image potential and M*ode* tells weather there are mobile electrons in the vicinity of the cations

Negative **A** indicates local charge density increase as a result of product formation. This is seen with several of the Zap data as opposed to Wyodak. With the successive loss of water there is a change in the local environment of the cations : $\pi \rightarrow \delta \rightarrow \pi$ with wet Zap and $\delta \rightarrow \delta \rightarrow \pi$ with wet Wyodak suggesting a somewhat different water-coal interaction in Zap as compared to Wyodak. Differences in *Mode* between dry samples are also evident. Both cations and water are thought to reside mainly at carboxylic sites (10-11). Water in coal participates in hydrogen bonding and delocalization in the π mode by definition involves a larger section of the coal molecule. Therefore in wet Zap the $\pi \rightarrow \delta$ change with water loss and negative **A,** or in other words the appearance of local charge at the carboxylic site, supports an earlier notion (12), that in Zap lignite charge transfer as a result of hydrogen bonding with water is significant.

What is happening to the demineralized coal in the absence of cations? If water is added, the carboxylic hydrogens will form hydrogen bonds with water, and the sites may be either hydrogen donor or acceptors depending on the electro negativity difference between water and the macromolecule. The polarity of the hydrogen bond or charge transfer accompanying hydrogen bond formation depends on the electronegativity difference, ΔE_n between the two partners. If there is mobility of charge in the vicinity, ΔE_n gradually decreases as more and more of these sites forms hydrogen bonds until $\Delta E_n \approx 0$. This occurs when all of the available active sites are depleted or, in other words at the monolayer saturation (13,14). If more water is added, hydrogen bonds starts forming between the second and first layer of water changing the direction of charge transfer. As a result the hydrogens acquire opposite charge. Since the boundary conditions in this model do not specify the exact geometry at the carboxylic sites, the parameters in Table 3. should be applicable to the carboxylic hydrogens too The carboxyl hydrogens are thought to be involved in hydrogen bonding, therefore the ionic radius is not known. Note that hydrogens in hydrogen bonds represent a charge distribution rather than a local charged sphere like cations. Therefore, using the parameters in Table 3., an "effective charge-effective radius" function for the carboxylic hydrogens, Ψ_H (u_{eff},a_{eff}) was calculated from the normalized product yields of the demineralized coals and the results are shown in Fig.2-5.

It is seen from Fig.2, that this shift really occurs from negativ through zero to positively charged hydrogen in Zap while it does not occur with Wyodak. Interestingly, the difference between Zap and Wyodak carboxyl hydrogens vanishes in dry coal suggesting a s

tructural change in both cases as a result of drying. While the carboxyl hydrogens are neutral during tar formation in Wyodak, they are positive in Zap suggesting a reaction path more ionic in nature.

The difference between pyrolysis and liquefaction is the strong hydrogen donation towards the coal molecule before and during fragmentation. As seen from Fig.5., this results in the disappearance of the difference between Zap and Wyodak as compared to pyrolysis.

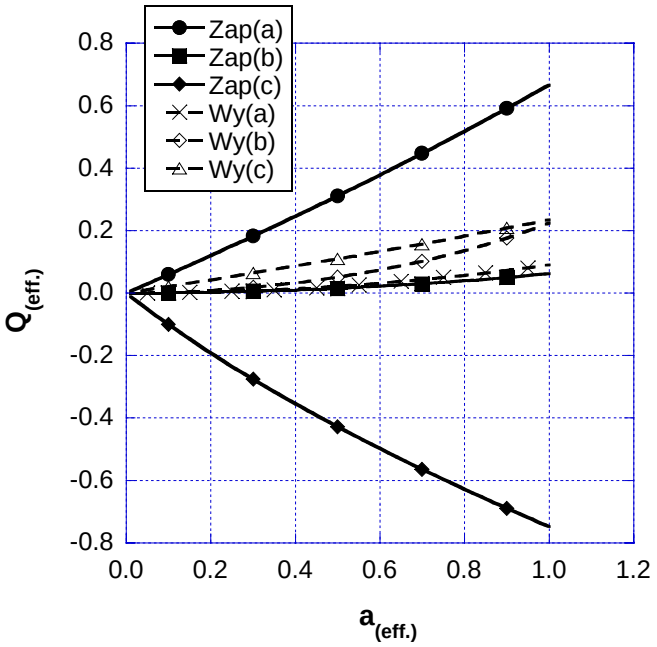

Figure 2. $\Phi_H(u_{eff.},a_{eff.})$ functions calculated from water evolutions of wet demineralized coals.

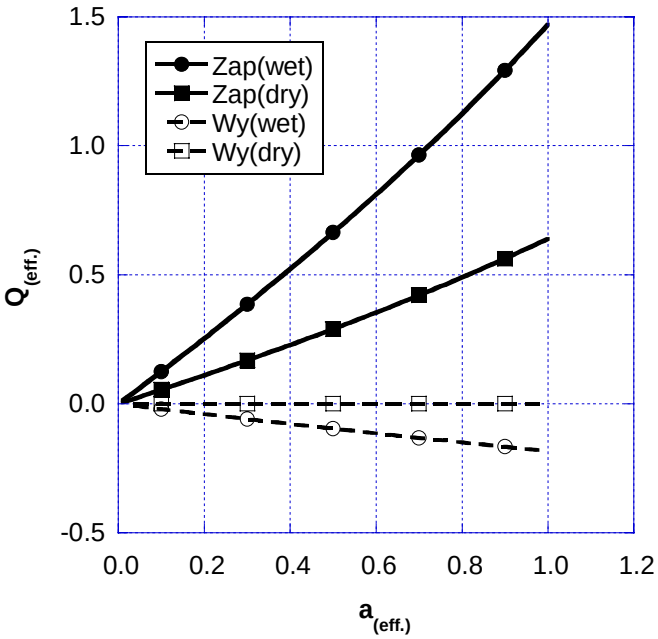

Figure 4. $\Phi_H(u_{eff.},a_{eff.})$ functions calculated from tar evolutions of wet and dry demineralized coals.

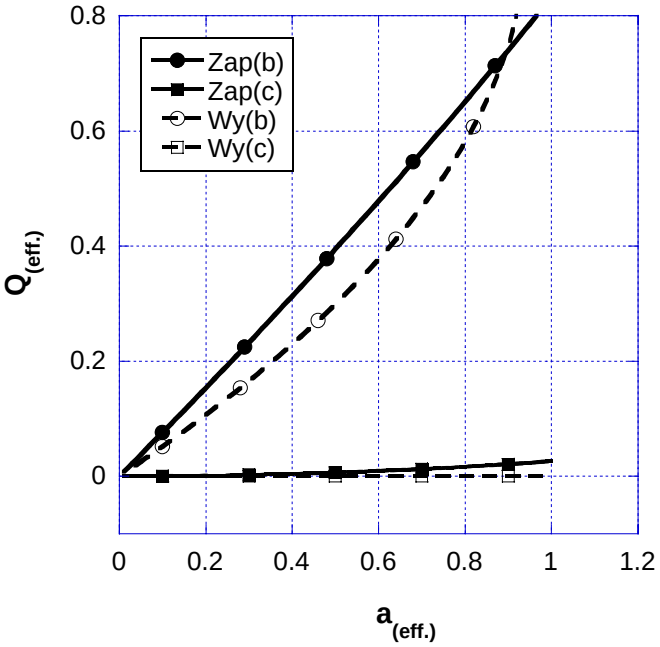

Figure 3. $\Phi_H(u_{eff.},a_{eff.})$ functions calculated from water evolutions of dry demineralized coals.

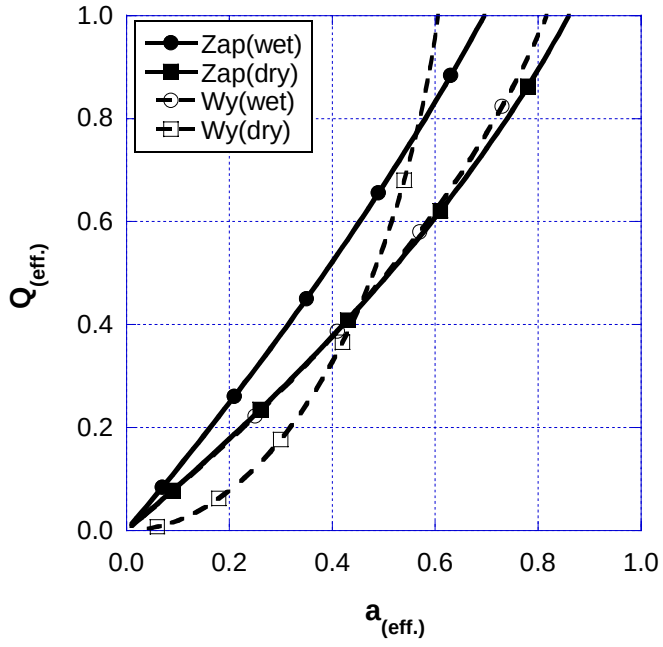

Figure 5 $\Phi_H(u_{eff.},a_{eff.})$ functions calculated from liquefaction asphaltene yields of wet and dry demineralized coals.

Conclusions

Demineralized and ion exchanged Zap lignites and Wyodak subbituminous coals was

described, in terms of product yield dependence on exchanged cation, as a large polymer single molecule. Based on the assumption that the exchanged cations can be treated as sources of local potentials, the single molecule treatment predicted linear correlation between these potentials and product yields. This was substantiated by experimental water evolution, pyrolysis tar and liquefaction asphaltene yields. An earlier suggestion, that hydrogen bonding is associated with significant charge transfer, was also demonstrated.

Acknowledgement

I gratefully acknowledge the extensive and useful discussions with M.A.Serio and Professor E.Suuberg from Braun University. Without those early stage reviews of the original ideas this work would not have been possible. I also thank for the data made available for me by H Teng and R Bassilakis.

References

(1) Painter.P.C.; Energ.Fuels **1996,** 10, 1273.
(2) Takanohashi,T.; Iino,M.;Nishioka,M. Energ.Fuels **1995,** 9, 788.
(3) TakanohashiT.; Nakamura,K.; Terao,Y.; Iino,M. Energ.Fuels **2000,** 14, 393.
(4) Noringa,M.;Iino,M. Energ.Fuels **2000,** 14, 762.
(5) Sereo,M.A.;Kroo,E.;Teng,H.;Charpenay,S.;Solomon,P.R. Prep.Pap.-Am.Chem.Soc.,Div.Fuel.Chem. **1993**, 38(2), 577.
(6) Carangelo,R.M.;Solomon,P.R.;Gerson,D.J. Fuel **1987**, 66, 960.
(7) Serio,M.A.;Solomon,P.R.;Bassilakis,R.;Kroo,E.;Malhotra,R.,McMillen,D. **1989**, Topical Report for PETC, Contract No. DE-AC22-88PC88814
(8) Hohenber),P.;Kohn,W. Phys.Rev. **1964**, 136:B864
(9) Chazalviel,J.N. Coulomb Screening by Mobile Charges Birkhauser Boston **1999**; pp 292.
(10) Schafer,H.N.S. Fuel **1980,** 59, 19.
(11) Nishino,J. Fuel **2000,** 80, 757.
(12) Kroo,E.; Prep.Pap.-Am.Chem.Soc.,Div.Fuel Chem. **1999,** 4(3), 637.
(13) Suuberg,E.M.;Otake,Y.;Deevi,S.C.;Yun,Y. Int.Conf.on Coal Sci.Proc. Butterworth-Heinemann Ltd. **1991**, pg.36.
(14) Lynch,L.J.;Barton,W.A.;Webstert,D.S. Int.Conf.on Coal Sci.Proc. Butterworth-Heinemann Ltd. **1991**, pg.8.

PYROLYSIS PROCESSING OF ANIMAL MANURE TO PRODUCE FUEL GASES

Michael A. Serio, Rosemary Bassilakis, Erik Kroo, and Marek A. Wójtowicz

Advanced Fuel Research, Inc.
87 Church Street
East Hartford, CT 06108-3728 USA

Introduction

Agricultural activities produce large quantities of animal wastes in the form of manures [1,2,3,4]. While some of the manure can be used as fertilizer, not all of it can be consumed in this way and the excess is an environmental liability. Another possibility is to use the manure as a direct or indirect source of fuel for remote power generation [5]. The use of animal manure for fuel has several benefits:

- Inexpensive – cheaper than propane, most natural gas, and electricity
- Avoids the cost of disposal
- Reduces odor and other nuisances associated with large livestock and poultry operations
- The potential applications of the energy-from-manure concept include space heating, steam, and electricity.

The conversion options include combustion, gasification, pyrolysis, and anaerobic digestion. Anaerobic digestion produces a biogas which has a heating value of 600-800 Btu/ft^3, which is 60-80% of the energy value of natural gas. This gas can be used to generate electricity, as a boiler or furnace fuel or to run refrigeration equipment. Gasification can produce a biogas with a heating value of 100-200 Btu/ft^3, only 10-20% of the value of natural gas. This low Btu gas is known as producer gas and can be used in any gas-fired appliance.

Direct combustion is also a possibility, although most fresh manures usually have too high a moisture content to burn and must be dried first. A direct combustion process can be used to produce process or space heat for small scale operations. Large scale operations can be used to produce electricity if the fuel is burned in a boiler and a steam turbine is used.

In the current study, the use of a staged pyrolysis process to produce medium Btu fuel gases (350 – 550 Btu/ft^3) for remote biomass power generation was investigated. This approach has several advantages when compared to more conventional processes:

- It has a higher process throughput than anaerobic digestion.
- It does not consume large quantities of water which must be treated, as in the case of anaerobic digestion.
- It can be used with poultry litter, an abundant resource, which is not as well suited to digestion because of its high lignocellulosic content.
- It can produce a higher Btu gas than conventional gasification processes.
- It can be more easily used with small scale power generation technologies than direct combustion and does not convert as much of the manure nitrogen to NO_x.

While many pyrolysis studies have been done on biomass materials [6-17], most of these have focused on plant biomass instead of animal manures and on the production of liquid fuels, chemicals, or hydrogen, and not fuel gas mixtures (H_2, CO, CH_4).

Animal manures are produced in abundance in the U.S. from several sources (cattle, hogs, pigs, sheep, lambs, layers, broilers, and turkeys). The 1995 estimates of livestock and poultry manures generated in the U.S. were 307x10^6 dry tons/year with an energy potential of 4.6 EJ/year [9]. This compares to total U.S. energy consumption of about 80 EJ/year [9]. Due to the economics of scale, farm animal production has gradually evolved in the direction of larger units, especially in the case of poultry. These concentrated animal populations generate large quantities of manure or litter, but often do not have the ability to use these materials on site for plant nutrients. In fact, manure becomes a liability for the large scale animal production facility instead of a benefit as it was historically on smaller farms. Since manure management has become a lower priority on larger farm operations, this has led to environmental problems such as water pollution and odors.

The fastest growing animal populations in the U.S. are the chickens which are raised for meat production (broilers) with an estimated population of 7018 x 10^6 in 1994 [9]. However, this was a 20% increase from 1990 and a 57% increase from 1985. The manure production averages 0.0403 dry kg/head-dry or 103.2 x 10^6 dry tons per year, equivalent to a human population of 983 million people! These data are summarized in Table 1, adapted from Reference 9, along with data for other types of manures.

Experimental

Samples of 5 manure samples were obtained as candidate materials. These included 2 samples of chicken manure (one broiler, one layer), turkey manure, cow manure, and seabird manure. The ultimate analysis data are provided in Table 2. The chicken manure samples are assumed to be mixed with small amounts of sawdust and should be considered "litters." The turkey manure sample was identified by the supplier as a litter. The seabird manure is believed to be a pure manure. The cow manure sample was dehydrated.

The individual manure samples were subjected to primary pyrolysis studies in a thermogravimetric analyzer with FT-IR analysis of evolved gases (TG-FTIR) at a heating rate of 30 K/min [18,19]. For the chicken #1 sample, additional runs were done at lower (3 K/min) and higher (100 K/min) heating rates for kinetic studies. A summary of the 30 K/min data (average of 3 runs) for all of the samples is given in Table 3.

It can be seen from the results in Table 2 that the ash content decreases in the order cow > turkey > seabird > chicken #2 > chicken #1. The moisture content decreases in the order cow > seabird > chicken #1 > chicken #2 > turkey. Based on considerations of a relatively high volatile matter and low ash and moisture contents, the chicken #1 (broiler) sample was selected as the best sample for more extensive testing. This selection was also based on the large resource potential of chicken manure (see Table 1). Both chicken manure samples were closest in elemental composition to wheat straw, which is a standard plant biomass material. Of course, all of the manure samples have higher nitrogen and sulfur contents than the wheat straw sample, although both of the chicken manure samples were among the lowest.

The TG-FTIR system that was used was subsequently equipped with a post pyrolyzer attachment and run at temperatures of 600, 800, 900 and 1000 °C for the chicken #1 sample and residence times of about 0.5 s. A second two-stage reactor was used to run larger samples with the second stage maintained at temperatures from 1050 to 1150 °C. The latter system was developed for NASA for pyrolysis of mixed waste materials in space [20,21].

The product yields for chicken #1 from the TG-FTIR system with a post pyrolyzer are shown in Table 4. These results indicate a progressive increase in CO, CO_2, CH_4, C_2H_4, NH_3 and HCN and a reduction in tar and oxygenated volatiles (formic acid, acetic acid, CH_3OH, formaldehyde, acetaldehyde, acetone, HNCO) as the temperature increases. H_2O appears to go through a maximum. The H_2 yield is not measured by FT-IR, but normally follows the trend of the CO yield (see below). These changes are the result of secondary

Table 1 - Livestock and Poultry Manures Generated in the United States and their Human Population Equivalents [9]

		Manure production		Human population equivalent	
Livestock/Poultry	Population (10^6)	(dry kg/head-day)	(10^6 dry t/year)	Factor	(10^6)
Cattle	103.3	4.64	174.9	16.4	1694
Hogs and pigs	59.6	0.564	12.3	1.90	113
Sheep and lambs	8.9	0.756	2.5	2.45	22
Layers	377.5	0.0252	3.5	0.14	53
Commercial broilers	7018	0.0403	103.2	0.14	983
Turkeys	289	0.101	10.7	0.14	40

[a] U.S. Dept. of Agriculture (1995) for population data. Populations of cattle, hogs and pigs, and sheep and lambs are for 1995; remaining populations are for 1994. With the exception of the commercial broiler population, other populations are assumed to be steady-state values because the variations are relatively small for each of the proceeding 10 years.

Table 2 - Elemental Analysis of Manure and Wheat Straw (Reference) Samples*

Sample	Basis	Moisture	Ash	C	H	O	S	N
Chicken I[a]	AR	11.4						
(broiler)	D		22.1	37.0	5.0	30.8	0.8	4.3
	DAF			47.4	6.5	39.5	1.0	5.6
Chicken II[b]	AF	9.6						
(layer)	D		36.3	29.4	3.8	25.2	0.8	4.6
	DAF			46.1	6.0	39.5	1.2	7.2
Turkey[c]	AF	6.0						
	D		52.3	21.5	2.7	14.9	3.3	5.2
	DAF			44.8	5.7	31.8	6.9	10.8
Seabird[d]	AF	13.2						
	D		36.4	18.3	3.4	24.1	2.2	15.6
	DAF			28.8	5.3	37.8	3.4	24.7
Cow[e]	AF	24.5						
	D		74.0	13.2	1.8	8.5	0.6	1.9
	DAF			50.5	7.1	32.8	2.3	7.3
Wheat Straw	AF	7.9						
(NIST)	D		9.0	43.7	5.6	40.9	0.2	0.6
	DAF			48.0	6.2	44.9	0.2	0.7

Notes: AR = As-received; D=Dry; DAF=Dry, Ash Free
*determined by Huffman Laboratories (Golden, CO)

a-Plant Right (Purdy, MO); b-The Real Poop (Chesapeake, VA); c-The Guano Company International (Cleveland, OH); d-Sustane (Cannon Falls, MN); e- Bovung (Assinippi, MA).

Table 3 – Average Results from Primary Pyrolysis Experiments at 30 °C/min in TG-FTIR System

Sample	Chicken Pellets I	Chicken Pellets II	Turkey Manure	Seabird Pellets	Cow Manure
Moisture	11.2	8.8	5.6	12.7	26.0
Ash	18.3	32.1	46.1	28.4	52.7
Volatile Matter	59.1	52.5	46.6	57.3	17.2
Fixed Carbon	11.4	5.9	2.1	1.8	4.0
Tars	28.55	24.37	31.78	3.31	9.06
CH_4	0.98	0.76	0.72	0.32	0.74
H_2O (pyr)	18.72	15.87	18.01	16.48	19.93
CO_2	14.27	24.77	18.26	18.90	24.87
CO	6.37	8.65	15.11	9.95	15.64
C_2H_4	0.25	0.29	0.25	0.95	0.13
SO_2	0.08	0.06	0.38	2.46	0.49
COS	0.61	0.37	1.77	3.12	0.58
NH_3	1.91	1.92	3.10	10.00	0.93
HCN	1.21	1.66	1.52	5.64	1.46
Formic Acid	0.72	0.39	0.27	1.96	0.00
Acetic Acid	1.63	1.48	0.36	0.00	0.50
CH_3OH	0.10	0.02	0.02	0.00	0.47
Formaldehyde	0.00	0.03	0.00	0.00	0.54
Acetaldehyde	6.31	4.66	4.85	2.95	2.57
Acetone	1.04	1.20	1.33	2.02	0.72
HNCO	1.42	2.58	1.53	16.75	0.86
NO	0.00	0.00	0.00	0.00	1.42

Notes: Yields are given on dry; ash-free wt.% basis except for moisture, ash, volatile matter, and fixed carbon which are given on an as-received basis.

cracking and gasification reactions and the net result is to increase the heating value. These results demonstrate the strong effect of secondary pyrolysis temperature on the gas composition and yield.

The NASA two-stage reactor system could be operated over a relatively narrow range of temperatures for the second stage (1050-1100 °C) in the case of the poultry manure sample, so the results, shown in Table 5, do not show as much variation. At a similar temperature level, the yields of CO_2 and CH_4 appear lower, while the yields of CO and H_2O are similar to the results from the TG-FTIR system (Table 4). The most notable difference was the much lower yields of C_2H_4 and HCN in the NASA two-stage reactor. This is believed to be the result of the catalyst (xerogel) bed in the second stage.

In the NASA reactor, yields for H_2 were reported in the 0.5 – 1.6 wt.% (as-received basis) range. These yields are determined by the difference between the total gas flow rate (minus the N_2 carrier) and the sum of the gases determined by FT-IR analysis, so they are less accurate than the other gas concentration measurements. The yields of H_2 are lower than what is obtained from a plant biomass sample with a similar elemental composition (wheat straw) by a factor of two [20]. This is probably due to the fact that much of the hydrogen in the starting sample ends up as NH_3 in the product gas.

The lower yields of H_2 with respect to wheat straw appear to be compensated for by much higher yields of C_2H_4, which will add to the heating value of the gas. This is especially true in the case of the TG-FTIR experiment with the post-pyrolyzer attachment (see Table 4), i.e., a homogeneous cracking zone.

The as-received char yields are higher (~40 wt.%) in the case of the two-stage reactor, in which the poultry manure pellets were pressed into pellets of approximately 16 g each. This contrasts with the ~30 wt.% yields (fixed carbon plus ash) from the TG-FTIR system, where the sample size is only 30-50 mg. These results suggest that higher fuel gas yields will be achieved by reducing the particle size.

The results of both reactors suggest that the product gas composition (in mole %) will be in the following ranges after condensing out water and NH_3: 15-25% CO, 10-20% CO_2, 25-40%H_2, 5-10% CH_4, 5-15% C_2H_4, <2% HCN, <1% H_2S. Consequently, it appears feasible to produce a medium Btu fuel gas (350-550 Btu/ft^3) from pyrolysis of poultry manure.

The chars collected from both reactor systems were quite reactive, indicating that char combustion to provide process heat should not be difficult. The reactivity is probably enhanced by minerals present in the manure.

Conclusions

Pyrolysis is an interesting alternative to land application or incineration of animal manures. Chicken manure appears to be well suited to this approach because of its relatively low ash and moisture contents and its availability in significant quantities at many locations in the United States. A combination of primary and secondary pyrolysis processing is able to produce a medium Btu fuel gas.

Acknowledgements

The authors gratefully acknowledge the financial support of the U.S. Department of Energy under Grant No. DE-FG02-00ER82936 and the technical advice and encouragement of the DOE Project Officer, Dr. Sam Tagore. The authors wish to thank John Fisher of NASA Ames Research Center for permission to use the NASA pyrolyzer constructed under Contract No. NAS2-00007

Table 4 - Results from TG-FTIR Experiments with Post Pyrolyzer Attachment for Chicken #1 Sample.

Post Pyrolyzer Temperature Run Number	**600 C AFR3811**		**800 C AFR3810**		**900 C AFR3809**		**1000 C AFR3808**	
	Product Yields (wt.%)							
	a.r.	daf	a.r.	daf	a.r.	daf	a.r.	daf
Moisture	7.7		7.9		9.1		11.4	
Ash (a.r.)	20.6		18.8		20.1		18.9	
Ash (dry)	22.3		20.4		22.1		21.3	
VM	60.7	82.81	60.0	81.86	58.3	82.3	58.1	83.36
Fixed Carbon	11.0	15.01	13.3	18.14	12.5	17.7	11.6	16.64
Tar	20.00	27.29	1.79	2.44	0.00	0.00	0.00	0.00
CH_4	0.67	0.91	1.70	2.32	2.15	3.04	2.42	3.47
H_2O (pyr.)	13.90	18.96	17.20	23.47	14.70	20.76	12.10	17.36
CO_2	11.10	15.14	14.51	19.80	15.36	21.69	17.29	24.81
CO	4.96	6.77	9.51	12.97	10.22	14.44	12.89	18.49
C_2H_4	0.23	0.31	1.70	2.32	6.02	8.50	6.39	9.17
SO_2	0.00	0.00	0.04	0.05	0.05	0.07	0.07	0.10
COS	0.33	0.45	0.14	0.19	0.00	0.00	0.00	0.00
NH_3	1.17	1.60	1.10	1.50	1.15	1.62	1.21	1.74
HCN	0.75	1.02	0.85	1.16	1.20	1.69	1.54	2.21
Formic Acid	0.24	0.33	0.00	0.00	0.00	0.00	0.00	0.00
Acetic Acid	1.10	1.50	0.00	0.00	0.00	0.00	0.00	0.00
CH_3OH	0.07	0.10	0.12	0.16	0.00	0.00	0.00	0.00
Formaldehyde	0.30	0.41	0.40	0.55	0.11	0.16	0.00	0.00
Acetaldehyde	4.57	6.23	0.58	0.79	0.00	0.00	0.00	0.00
Acetone	1.32	1.80	0.23	0.31	0.17	0.24	0.05	0.07
HNCO	1.11	1.51	0.82	1.12	0.81	1.14	0.62	0.89
NO	0.00	0.00	0.00	0.00	0.00	0.00	0.00	0.00
sum of volatiles	61.82	84.34	50.69	69.15	51.94	73.36	54.58	78.31
difference between balance and gasses	-1.12	-1.53	9.31	12.70	6.36	8.98	3.52	5.05

Notes: All yields are expressed in grams of a given product per gram of initial sample * 100% on as-received (a.r.), dry (dry), and dry, ash-free (daf) bases.

Table 5 - Results from NASA Two-Stage Pyrolyzer Experiments with Chicken #1 Samples*

Post Pyrolyzer Temperature	**1100 °C**	**1100 °C**	**1100 °C**	**1100 °C**	**1100 °C**	**1050 °C**
Run Number	22	23	24	25	26	27
Char	41.1	40.7	40.8	40.8	40.7	41.1
H_2O	12.3	14.6	13.1	15.3	15.2	12.4
Carbon	0.8	2.6	9.2	2.8	4.1	9.1
Trap & Filter	4.7	4.5	2.9	2.8	3.9	14.1
Gases	41.0	38.2	37.8	38.6	36.3	23.4
H_2	1.6	0.6	0.5	1.2	0.7	1.1
C_2H_4	0.4	0.3	0.4	0.3	0.3	0.3
CH_4	3.0	3.0	3.3	3.6	3.0	1.7
CO_2	23.0	21.0	20.2	19.7	19.0	15.1
CO	13.0	13.3	13.4	13.8	13.3	5.2
NH_3	1.5	1.3	<0.1	1.2	2.4	1.2
HCN	0.3	<0.1	<0.1	0.3	<0.1	0.5

*results are given on an as-received basis; char = fixed carbon plus ash

for animal manure samples. We are also grateful to Prof. Eric Suuberg of Brown University for valuable discussions.

References

1 Barrier, T.W., and Bulls, M.M., "Feedstock Availability of Biomass and Wastes," Chapter 23, in ACS Symposium Series No. 476, ACS Washington, DC pp. 410-421.

2 Chartier, P., Ferrero, G.L., Henius, V.M., Hultberg, S., Sachau, J., Wiinblad, M., "Biomass for Energy and the Environment: Proceedings of the 9th European Bioenergy Conference," Pergamon, New York (1997).

3 Stanford Research Institute, "An Evaluation of the Use of Agricultural Residues as an Energy Feedstock," Vol. 1, National Science Foundation Grant No. AER74-18615 A03, NSF/RANN/SE/G1/18615/FR/763 (1976).

4 Gerwig, B.K., Hegg, R.D., "Assessment and Characterization of Manure in the Southeaster U.S.," Proceedings of Bioenergy '96, pp. 501-507, Sept. 15-20, 1995.

5 The Ohio Biomass Energy Program, Grant No. CGLG-98-018, "Turning Manure Into Gold: Converting Agricultural Waste to Energy."

6 Rowell, R.M., Schultz, T.P., Narayan, R., "Emerging Technologies for Materials and Chemicals from Biomass," ACS Symp. Series No. 476, ACS Books, Washington, DC (1992).

7 Dayton, D.C., Chum, H.L., "Symp. on Biomass Fuels: The Introduction," Energy & Fuels, 10(2), 267 (1996).

8 Wang, D., Czernik, S., Montané, D., Mann, M., Chornet, E., Ind. Eng. Chem. Res., 36, 1507 (1997).

9 Klass, D.L., Biomass for Renewable Energy, Fuels, and Chemicals, Academic Press, New York (1998).

10 Bridgewater, A.V., *Biomass*, 22, (1-4), 279 (1990).

11 Antal, M.J., Jr., in Adv. in Solar Energy (Boer, K.W., Duffie, J.W., Eds.), American Solar Energy Society, Boulder, CO, 1, 61 (1984); 2, 175 (1985).

12 Shafizadeh, F., in The Chemistry of Solid Wood (R. M. Rowell, Ed.), Advances in Chemistry Series No. 207, American Chemical Society, Washington, DC (1984).

13 Bridgwater, A.V., and Cottam, M.-L., Energy and Fuels, 6, (2), 113 (1992).

14 Elliott, D.C., Beckman, D., Bridgwater, A.V., Diebold, J., Severt, S.B., and Solantusta, Y., Energy and Fuels, 5, 399 (1991).

15 Overend, R. P. Milne, T. A., and Mudge, L.K., Eds., Fundamentals of Thermochemical Biomass Conversion, Elsevier, (1985).

16 Soltes, E.J., and Milne, T.A., Eds., Pyrolysis Oils from Biomass: Producing, Analyzing and Upgrading, ACS Symposium Series No. 376, American Chemical Society, Washington, DC (1988).

17 Bridgwater, A.V., Kuester, J.L., (Eds.), Research in Thermochemical Biomass Conversion, Elsevier Applied Science, London (1988).

18 Carangelo, R.M., Solomon, P.R., and Gerson, D.G., Fuel, 66, 960 (1987).

19 Carangelo, R.M., Solomon, P.R., Bassilakis, R., Gravel, D., Baillargeon, M., Baudais, F., and Vail, G., American Laboratory, P. 51, (1990).

20 Chen, Y., DiTaranto, M., Wójtowicz, M.A., Marran, D. and Serio, M.A., Final Report for NASA Phase I, Contract No. NAS2-99001 "Pyrolysis Processing for Solid Waste Resource Recovery in Space," June 1999.

21 Serio, MA., Kroo, E., Bassilakis, R., Wójtowicz, M.A., and Suuberg, E.M., "A Prototype Pyrolyzer for Solid Waste Resource Recovery in Space," 31st International Conference on Environmental Systems, Orlando, FL, July 9-12, 2001, SAE paper No. 2001-01-2349.

SLURRY INFLUENCE OVER THE VISBREAKING PROCESS

Carrillo J.A., and Garzón G.
ECOPETROL-Instituto Colombiano del Petróleo Km 7
Bucaramanga, via a Piedecuesta, Colombia S.A.

Introduction

The Visbreaking is a process of thermal cracking applied to the barrel bottoms, being this vacuum bottoms or deasphalting bottoms (DEMEX bottoms). This is a process used to reduce the viscosity [1, 2]. The severity limit in the visbreaking is determined by the fuel oil stability and by the coke production [3]. In this study we present the results of processing different quantities of slurry into the visbreaking feed. We found that with the increase in the slurry content in the feed, to reach the same conversion we should decrease the furnace temperature. In addition to that we notice that the light cycle oil (LCO) in the feed produces an increase in the distillate production. The addition of slurry to the feed causes a reduction in it viscosity in higher amount than expected just for dilution. It means a positive change in the colloidal equilibrium of the system [4-6].

Methodology.

For this study it was applied the methodology reported in [7]. The feed was DEMEX bottoms. There were prepared samples with 0, 10, 15 y 20 wt % of slurry and 8 wt % of LCO, and in addition to that there was a sample with no slurry and with no LCO. All the feed samples were characterized and compared. To have a reference point, the sample with no slurry and with no LCO was run at different temperature condition and its products were analyzed. Then the samples with different concentration of slurry and with 8 wt % of LCO were run at the visbreaking pilot plant. In all the runs at pilot plant level it was maintained constant steam (0.4 wt %) and reaction time (1,3 minutes). The tested temperature points were: 468, 476, 481 y 485 °C.

Results:

1. Feed

From fig. 1 and table 1 we can see that as the slurry concentration in the feed is increased, the viscosity, sulfur, CCR and insolubles in the feed decrease and VBN increases according to the equations:

Viscosity @ 177 °C $y = -0.0076x^2 - 0.1011x + 6.3467$ $R2 = 0.8702$

Viscosity @ 190 °C $y = -0.0113x^2 + 0.042x + 3.5442$ $R2 = 0.9731$

Sulfur $y = -0.0202x + 2.3194$ $R2 = 0.8042$

CCR $y = -0.2859x + 33.194$ $R2 = 0.9809$

Insolubles i nC_7 $y = -0.0068x2 - 0.1836x + 23.368$ $R2 = 0.945$

VBN $y = 0.0115x2 + 0.0206x - 3.3122$ $R2 = 0.8783$

x- slurry concentration, wt.

Up to 10 wt % of slurry concentration in the feed, the changes in the viscosity, insolubles and VBN correspond to the straight line, but after that point the trend change to polynomial. It is possible that before 10 wt % concentration of slurry in the feed it behaves as simply diluent, and after that concentration it causes changes in the colloidal system that produces more reduction in viscosity, insolubles and VBN than expected as can be seen from fig. 1 and 2.

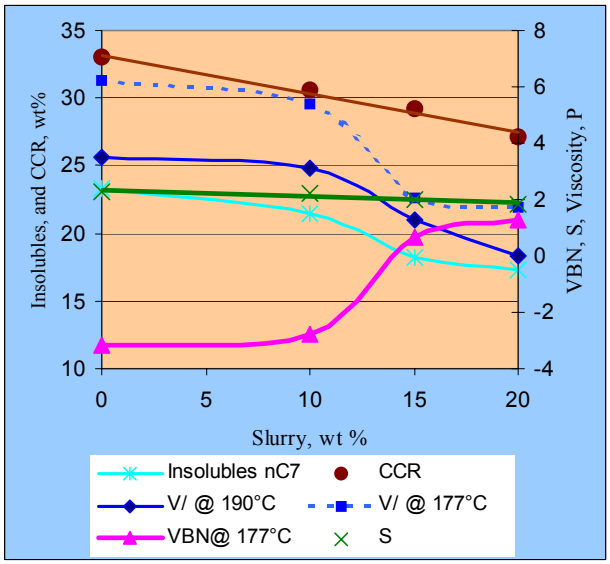

Fig. 1. Influence of slurry over the physical properties of the feed.

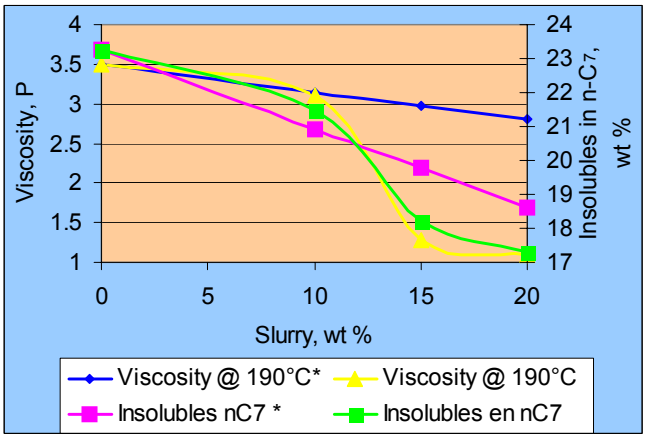

Fig. 2. Colloidal behavior of the mixture of feed with slurry; *- Expected values.

The other properties like CCR and sulfur maintain the same linear trend in the analyzed interval.

The correlation between insolubles in nC_7 and nC_5 is linear and correspond to the equation:

$y = 1.2986x + 4.0088$ $R2 = 0.9894$

y- insolubles in nC_5; x- insolubles in nC_7.

Another analyzed influence of dilution was the incidence of LCO and slurry over the simulated distillation. We found that with the addition of 8 wt % of LCO, the summa of light and heavy gasoils increases from 17.3 to 30.0 wt %, but the expectance was 25.3 wt %. It means that with the use of LCO we can increase the distillate production in the topping units. The addition of slurry increases de distillation production in the expected quantity.

2. Runs at visbreaking pilot plant.

To have a reference point there were held three runs with DEMEX bottoms without slurry, at three different temperatures. The results are shown in table 1. It was found that the reference feed could be processed up to 481 °C, and after that temperature the product is unstable by Merito Test.

Table 1. Severity by temperature (steam: 0,4 wt %; LCO: 8 wt %,; Slurry: 0 wt %; Feedstock: DEMEX bottoms; t: 5 min.)

T, °C	Merito test	Bottoms, wt %	Lights, wt %	Gases, wt %	Coke, wt %	Conversion, wt %
476	6	90.76	7.11	1.09	1.05	8.2
481	7	90.25	7.16	1.48	1.11	8.6
485	8	85.88	10.03	1.81	2.28	11.8

As the slurry concentration in the feed is increased, the reaction temperature (at which the maximum allowable conversion is reached) decreases, and the properties of the visbreaking bottoms such viscosity, CCR and sulfur decrease. As a result we have the following consequences:

- The decrease in the reaction temperature means an important fuel saving.
- The viscosity reduction or the increase in the VBN (Viscosity Blending Number) represents a reduction in the diluent needed for the fuel oil preparation.
- The higher concentrations of slurry in the feed (15 an 20 wt %) present a relative low ΔVBN, but at the same time they present low viscosity. For that reason they need the lowest quantity of LCO as diluent.
- The sulfur reduction as a consequence of slurry addition to the feed means a sulfur reduction in the fuel oil. It is one of the main purposes to reduce atmospheric pollution.

In the material balance, the conversion, corresponding to different concentration of slurry in the feed for all studied cases, is similar, but with the addition of slurry to the visbreaking feed we have:

- A reduction in the furnace coke production, that means longer runs
- The decrease in the visbreaking bottoms and increase in the Gas Oil production is caused by slurry dilution factor.

References

1. Savaya Z.F and others, 1989. "Stability of fuel Oil produced by visbreaking of vacuum residue" Fuel, V68, p1064-1066.
2. Zanker A., 1878. "Visbreaking resid? Figure value", Hydrocarbon Processing, November, p205-206
3. Yan T.Y., 1989. "Characterization of visbreaking feeds". ACS meetin. Dallas, April 9-14, p428-433.
4. Furlong L.E and others, 1976. "The Exxon Donor Solvent Process" CEP August p6975.
5. Bianco A.Del. and others, 1993. "Thermal cracking of petroleum residues: Hydrogen donor solvent eddition". FUEL, V72, January, p8185.
6. Michel T. And others, 1989. "Visbreaking of Safaniya vacuum residue in the presence of additives". FUEL, V68, March, p318-322.
7. J. A. Carrillo; J. Saavedra and L. G. Garzón, 2001. "Processing of slurry in the visbreaking unit". Fuel Division, 222nd National Meeting, August 26-30,

Table 2. Behavior of the different visbreaking bottoms produced at maximum allowable temperature

Feed			Visbreaking bottoms			Products, wt %					
Slurry wt %	T °C	Viscosity @ 375°C, cP	ΔVBN	S wt%	CCR wt %	Coke	Bottoms	Gas Oil	Naphtha	Gas	Conv
20.0	468	52	2.41	1.7	32.2	1.0	40.5	50.0	7.1	1.4	8.5
15.0	472	58	2.25	1.8	32.0	1.0	38.6	50.9	7.8	1.7	9.5
10.0	476	99	3.61	1.8	32.0	1.1	40.5	49.2	7.7	1.5	9.1
0.0	481	175	1.98	1.9	35.0	1.1	46.5	43.8	7.2	1.5	8.6

STABILITY OF COAL DERIVED SYSGAS COMBUSTION FOR THE APPLICATION IN IGCC SYSTEM

Hyung-Taek Kim and Byung-Chul Choi

Department of Energy Studies
Ajou University
San 5 Won Chun Dong Pal Dal Gu
Suwon, KOREA

Introduction

Developing integrated coal gasification combined-cycle systems ensures cost-effective and environmentally sound options for supplying future power generation needs. The reduction of NOx emissions and increasing the inlet temperature of gas turbines are the most significant issues in gas turbine development in IGCC power generation systems. The coal gasified fuel, which is produced in a coal gasifier of an O_2 blown entrained-flow type, has a calorific value as low as 1/10 of natural gas. The study is to report some systematic measurements of the flame stability limits of swirl-stabilized flames on coal gasified synthetic gas and to explain the measured trends using concepts that have been successfully used in nonswirling flames and previous study. The 2,000 kcal/hr class tangential air input type swirl diffusion burner was designed to hold stable combustion burning low-Btu gas and the combustion air are supplied into a fuel-lean combustion enclosure with swirl. The axial and tangential airs are properly mixed with combustion enclosure to react the oxidization of low-Btu gas reactants in fuel lean condition. By testing under atmospheric pressure conditions, the authors have obtained a very significant result through investigating the effect of a various experimental condition characteristics. Gaseous fuel by recent energy consumption trends in Korea, the demand for electric power generation has been further increasing. There are already plans to build more fossil fuel power plants as well as nuclear power plants. The combined-cycle power generation system is a system to combine a topping cycle gas turbine and a Rankine cycle steam turbine as bottoming components. Coal gasifier to gasify coal and to remove ash, clean-up mechanism to desulfurize produced coal gas and to remove dust, high temperature gas turbine, steam turbine, and exhaust heat recovery boiler. Another characteristic of the coal-gasified fuel is that it normally contains about 1000ppm NH_3, which is the source of fuel NOx. But these characteristics of fuel not included on the experimental conditions The amount of air for combustion is first calculated at a theoretical mixing ratio. To calculate air distribution, the overall amount of air is assumed to be varied from 100 percent to 200 percent. And results of these experiments compare with characteristic of pure hydrogen and methane flame by using previous theoretical or experimental formula on flame stability limit. The fuel gases used are various compositions of carbon monoxide and hydrogen. Burner diameters are consisted of 1.27, 1.93, and 2.95 mm on axial type fuel nozzles. The tangential type fuel nozzles are used 3 types on different shapes.

Experimental

A schematic of the laboratory scale swirl-stabilized diffusion burner apparatus is shown in **Figure 1**. Cylinder tank is used for producing predetermined composition of fuel gas and compressor is used for the delivery of air. Bottled coal syngas from 3 ton/day gasifier will be also fired for the comparisonal study. Flashback safety device is installed upstream of fuel gas inlet point. Once the flame is established, temperature is monitored by thermocouples. Concentrations of NOx and unburned hydrocarbon are also measured with chemiluminescent NOx analyzer and FTIR. The shape of each flame is also recorded with Image Capture Device.

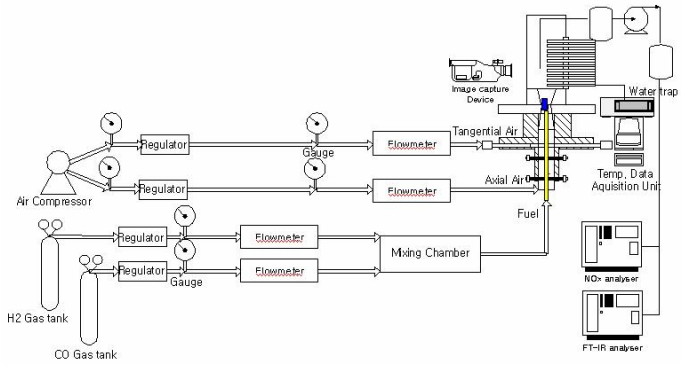

Figure 1. Schematic diagram of the laboratory scale burner

The swirl generator consists of four tangential air inlets that mix tangential air with axial air upstream of the burner. The swirling coaxial airflow surrounds a central fuel tube that injects fuel in the axial or tangential direction. But axial fuel injection is preferred to study flame stability limit because when the tangential fuel injection is really complicated to analyze characteristics of flame on low-Btu gas. Also the swirl is gradually reduced to zero, one recovers the important case of a jet flame with coaxial air that is documented in the literature; thus the swirl and no-swirl cases can be properly compared. Six different shaped fuel nozzles were used; their shapes and dimensions are given in **Figure 2**.

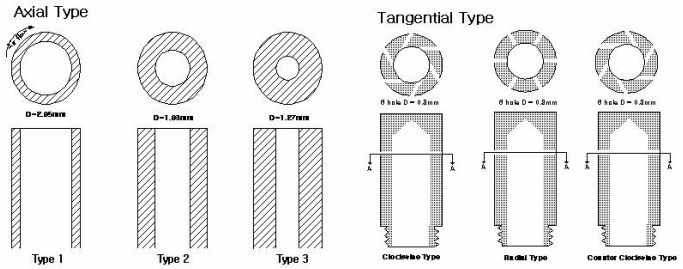

Figure 2. The fuel nozzle types on different shapes

In these cases the ratio of the fuel tube inner diameter, denoted d_F, to the air tube diameter d_A at the throat was different on the fuel nozzle shapes; the ratio of the fuel tube inner diameter to the outer diameter denoted d_F/d_{F0}. Eights different fuels were used; their properties are given in **Table 1**.

Table 1. Physical properties on different composition fuels

Gas	Purity/ Composition, %v	Molecular weight	Dynamic Viscosity, μ, at 0℃, micropoises	Maximum Burning Velocity in air, S_u, m/s	Mass fraction in stoichiometric mixture with air, θ_s
Methane	99	16	102.7	0.39	0.055
Hydrogen	99	2	84.2	3.06	0.028
Carbon monoxide	99	28	166	0.136	0.289
H_2 : CO	(1:1), 99	15	182.5	1.66*	0.179
H_2 : CO	(1:1.5), 99	17.6	184.8	1.41	0.204
H_2 : CO	(1:2), 99	19.42	185.7	1.23	0.220
H_2 : CO	(1.5:1), 99	12.4	178.7	2.02	0.153
H_2 : CO	(2:1), 99	10.58	174.7	2.20	0.133

Pure methane, pure hydrogen, pure carbon monoxide, a mixture of 0.5 hydrogen and 0.5 carbon monoxide by volume, a mixture of 0.4 hydrogen and 0.6 carbon monoxide by volume, a mixture of 0.34 hydrogen and 0.66 carbon monoxide by volume, a mixture of 0.6 hydrogen and 0.4 carbon monoxide by volume, and a mixture of 0.66 hydrogen and 0.34 carbon monoxide by volume, as listed in **Table 1**. Flow rates were metered using a system of calibrated gas meter and 4 rotameters. Flow rates were metered to an accuracy of 10%. Control of fuel velocity was calculated for experimental conditions and compressibility effects on system are considered. That is, for most cases fuel velocity U_F is determined by dividing measured fuel mass flow by the fuel tube area and by the standard density of the fuel gas. For the data, the exit Mach number of the fuel that was used was determined from standard compressible flow tables and the known stagnation pressure and temperature. To obtain recirculation vortex on combustion environmental, a diverging metal quarl section is placed downstream of the cylindrical throat. Upstream of the tangential air inlets, the axial air profile was assumed uniform flow. The swirl number S in the study is identical to the conventional definition given by Ref. 2, i.e., S is the ratio of the flux of angular momentum passing through the throat to the flux of axial momentum, divided by the throat radius.

Results and Discussion

Just prior to investigate flame stability limit, Different characteristics of flames were observed, first lifted flames, which look like lifted simple jet flames, second jet like flames, which look like long, attached jet flames but blow out suddenly without lifting off; third short flames, which also blow out suddenly without rising. But these flames not accurately divided on different characteristics. The stability limit for each nozzle was determined as follows. A low flow rate of fuel was delivered to the nozzle for start-up. An ignitor was used to ignite the fuel such that a diffusion type flame resulted. The fuel and the swirl air flow rates were slowly and alternately increased until the desired firing rate and excess air percentage were achieved or the flame blow out. If the flame was stable at the desired excess air percentage, the swirl air was decreased as the axial air was increased by an equivalent amount such that the total air flow to the burner remained constant. As the axial air was increased, the amount of swirl decreased. The point at which the flame extinguished indicated the blow off or stability limits of the flame at that excess air percentage and swirl ratio. To study changing effect a heating rate on burner, heating rate varied from 1,000 kcal/hr to 3,000 kcal/hr. These experiments were continued for increasing excess air ratios until a flame was no longer achievable under any swirl conditions. The flame stability limits for axial type fuel nozzle 1 is presented in **Figure 3**.

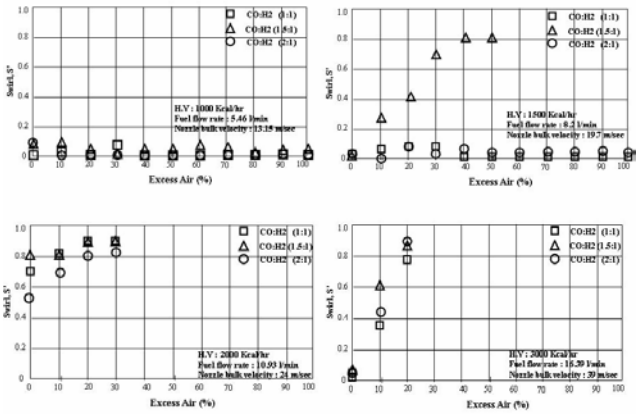

Figure 3. Flame stability limit for axial type 1 fuel nozzle

Considering heating rate for flame stability limit on same experimental conditions, the flame stability limit is gradually decreased with increasing heating rate. Flame stability region on 1000 kcal/hr class is not affected by variation of swirl number and excess air. The 3000 kcal/hr class compare with other heating rate conditions has relatively narrowed region. The flame stability limits for axial type fuel nozzle 2 and nozzle 3 are presented in **Figure 4** and **Figure 5**.

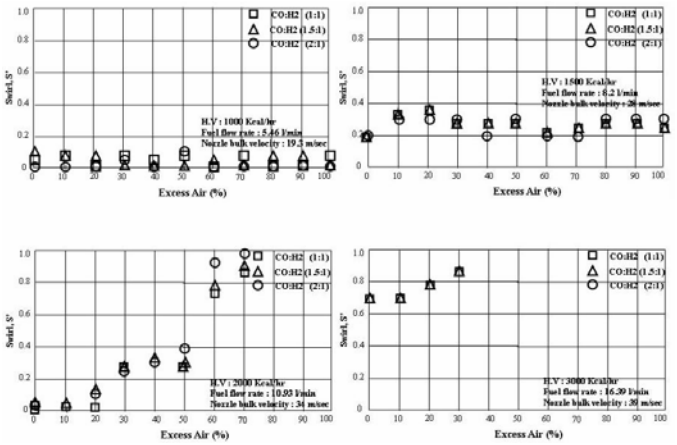

Figure 4. Flame stability limit for axial type 2 fuel nozzle

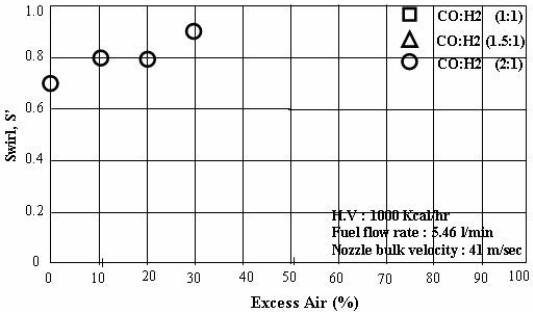

Figure 5. Flame stability limit for axial type 3 fuel nozzle

As shown by **Figure 5**, the axial type 3 nozzle can only by stabilized with all swirling air (S'>0.8) at 30% excess air. The axial type 1 and 2 nozzles with 1000 kcal/hr have the largest flame stability region. The axial type 3 nozzle that operates over 1500 kcal/hr experimental conditions can not be stabilized under any swirl or excess air conditions. whereas the axial type 1 and 2 fuel nozzles on 1000 kcal/hr experimental conditions have a much wider swirl stability range, e.g., $0.1 \leq S' \leq 1.0$ at entire excess air range. The effect of mixing gas variation on flame stability region does not found within axial type 1 and 2 experimental conditions. However the axial type 3 fuel nozzle which experiment on CO:H2 (2:1) only have flame stability region. The general shapes of flame on axial type of nozzles exhibit cone shape. As the excess air is increased, the flame length decreases for all experimental conditions. The axial type 1 and 2 fuel nozzle has a wider swirl stability range than the axial type 3 fuel nozzle for whole excess air range on 1000 kcal/hr. axial jet nozzles exhibit a type I flame structure due to the fuel jet penetration into the recirculation zone. For the smallest axial nozzles, the fuel jet fully penetrates the recirculation zone, resulting in a small blue, bulbous, off-axis recirculation zone at the base of the flame with a long yellow flamelet tail. As the amount of excess air is increased for high swirl

cases, the tail length and luminosity decrease as the recirculation zone size increases. At the lower swirl cases, the recirculation zone is less easily identified. For the largest axial nozzle, due to its lower fuel injection velocity, the fuel jet flamelet does not extend as far downstream of the recirculation zone boundary. Similar to the smallest and largest nozzle, as the excess air is increased at high swirl cases, the flame becomes wider, more blue and more compact.

The flame stability limits for tangential type fuel nozzles are presented in **Figure 6**. the flame stability results of tangential type fuel nozzles are only displayed 3000 kcal/hr experimental condition. Because experimental flame stability results on tangential type fuel nozzles have all of swirl and excess air range below of 3000 kcal/hr experimental condition.

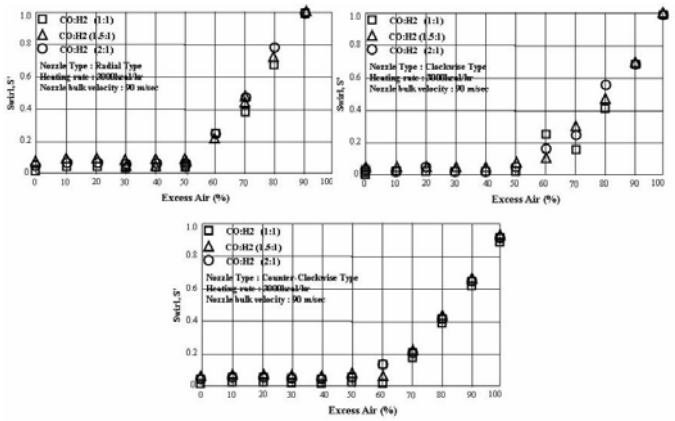

Figure 6. Flame stability limit for tangential type fuel nozzles

The radial type fuel nozzle held flame stability region non swirling air and excess air 50% and flame stability region is exponentially decreased over excess air 50%. The clockwise and counter-clockwise type fuel nozzles also have similar to flame stability trend of the radial type fuel nozzle. Relatively, for the tangential type fuel nozzles, the counter-clockwise fuel nozzle has the widest swirl stability range, e.g., $0.9 \leq S' \leq 1.0$ at 100% excess air. In reference to the IFRF flame classifications, as depicted in **Figure 6**, these flame structures correspond to a type II flame due to the outward (radial) fuel injection and correspondingly low fuel penetration. The tangential type fuel nozzles exhibit short, blue "petal-like" flames from each jet exit with a non-luminous inner core. At high swirl, the shear layer caused by the swirling air and entrained air forces the fuel jets outward to form thin petals. At lower swirl, the petals are closer to the centerline, due to the decreased expansion, and meld together forming less discrete jets. These flames are type II flames, again due to the off-axis, annular fuel injection and low fuel penetration in the recirculation zone.

Acknowledgment

Authors express special thanks to the researchers of Plant Engineering Center, Institute for Advanced Engineering (IAE) for the helpful comments during the course of this work. The financial support is from the R&D center of Korean Energy Management Corporation through the Energy R&D program of Ministry of Commerce, Industry, and Energy of Korean Government.

References

1. Matt Mikio Miyasato., Thesis, MA, University of California Irvine. **1993**
2. J. M. Beer., N. A. Chigier., Combustion Aerodynamics, Robert E. Krieger Publishing Company, INC. Malabar, **1983**
3. Byung-Chul Choi., Hyung-Taek Kim., Proceeding of 2001 KIChE Fall Meeting, p 4635-4638, **2001**

STRUCTURAL GROUP CONTRIBUTION METHOD FOR PREDICTING THE OCTANE NUMBER OF PURE HYDROCARBONS AND THEIR MIXTURES

Tareq A. Albahri

Chemical Engineering Dept.
Kuwait University
P.O.Box 5969
Safat 13060, Kuwait

Introduction

When the fuel-air mixture in the cylinder of a spark-ignition engine burns spontaneously in localized areas instead of progressing from the spark, this explosive decomposition produces a characteristic noise or knock. The accompanying pressure surge results in loss of power and fuel economy and may result in engine damage[1]. For these reasons, the antiknock quality of gasoline, normally expressed in terms of octane number, is one of their most important properties.

Since the quality of gasoline depends upon its composition, one could theoretically calculate the octane number from a comprehensive analysis of the individual hydrocarbons in gasoline and their contribution to the overall octane quality. Aside from the fact that a theory describing and quantifying the relationship between composition and octane number has not yet been fully developed, the major obstacles to this approach is in the lack of a method to obtain the compositional data and in the scarcity of octane number ratings for pure hydrocarbons. The former impediment is partially solved by the introduction of new analytical (gas and liquid chromatography) and theoretical techniques[2] while the latter which still awaits the introduction of new techniques for estimation, is solved in this work.

Technical Development

A careful examination of the octane rating of hundreds of hydrocarbons reveals its complex dependency on the molecular structure and makes it one of the most difficult properties to estimate or correlate using only the physical and chemical properties. In this work we investigate this structural dependency of octane number using a structural group contribution approach, already used for predicting many other physical and chemical properties[3].

The structural groups derived from the Joback group contribution approach[3], with some modification, are shown in Table 1. The research octane number is calculated using the following equation,

$$RON = \left[104.8 - 5.395\left(\sum_i (ON)_i\right) + 6.532\left(\sum_i (ON)_i\right)^2 - 5.165\left(\sum_i (ON)_i\right)^3 + 0.6189\left(\sum_i (ON)_i\right)^4 \right] \quad (1)$$

Where $\sum(ON)i$ is the sum of the group contributions listed in Table 1.

Data on the octane number of more than 200 pure hydrocarbons, most of which are in the gasoline boiling range from the API-TDB[4], were used to estimate the values of the various group contributions. An optimization algorithm based on the least square method, that minimizes the sum of the difference between the calculated and experimental RON data, was used for that purpose. The average deviation in the predicted octane numbers for all types of hydrocarbons, ranging in RON from -20 to 120, was 4 and the maximum was 26. The average percentage error was 6% and the correlation coefficient was 0.975. The model predictions for pure components are shown in Figure 1.

Table 1. Group contribution for estimation of octane number.

HC type	Serial no.	Group	$(ON)_i$
Paraffins	1	−CH3	0.459
	2	−C2H5	0.948
	3	>CH2	0.680
	4	α- >CH−	-0.139
	5	β- >CH−	-0.362
	6	δ- >CH−	-0.358
	7	α- >C<	-1.357
	8	β- >C<	-1.828
Olefins	9	=CH−	-0.078
	10	=CH− (C# ≥ 4)†	-0.660
	11	α- >C=	-0.811
	12	β- >C=	-0.6441
	13	=CH2	0.119
	14	=C=	2.693
	15	=CH− (-cis)	-0.409
	16	=CH− (-trans)	-0.387
	17	≡CH	-1.267
	18	≡C−	0.603
Cyclic[1]	19	>CH2	0.400
	20	>CH−	0.122
	21	>CH− (-ortho)	-0.330
	22	>C<	-0.800
	23	=CH−	-0.064
	24	>C=	-0.356
	25	C_3 ring correction	-1.132
	26	C_4 ring correction	1.18
	27	C_7 ring correction	0.702
	28	C_8 ring correction	-0.520
Aromatics§	29	=CH−	-0.202
	30	>C=	0.193
	31	>C= (-ortho)	-0.337
	32	>C= (-meta)	-0.959
	33	>C= (-para)	-0.498

§ Groups 19 through 29 are all non-fused.

† For a carbon atom that is fifth or higher order along the HC chain.

α-, β- and δ- refer to the 2nd, 3rd and 4th position on the HC chain respectively.

For multi component mixtures, a total of 560 randomly chosen sets of molecules with random compositions were used to assess the accuracy of the model predictions for octane numbers of well-defined mixtures and study the effect of the number of components in the mixture on the model correlation. For each of the 560 mixtures two sets of octane numbers are used for mixtures of 200, 100, 50, and 25 molecules. The experimental octane numbers were used in one set and the predicted octane numbers were used in the other. Kay's mixing rule using mole average was used to calculate the octane number of the mixtures and the two are compared. The number of tests for each set of molecules and the results are presented in Table 2. The model prediction for hydrocarbon mixtures is shown in Figure 2.

Table 2. Comparison of experimental and predicted octane numbers for multicomponent mixtures

No. of mixtures tested	No. of components per mixture	R^2	Average RON deviation	Maximum RON deviation
35	200	0.99997	0.25	0.7
105	100	0.9995	0.3	1.0
140	50	0.998	0.5	2.4
280	25	0.99	1.8	5.1

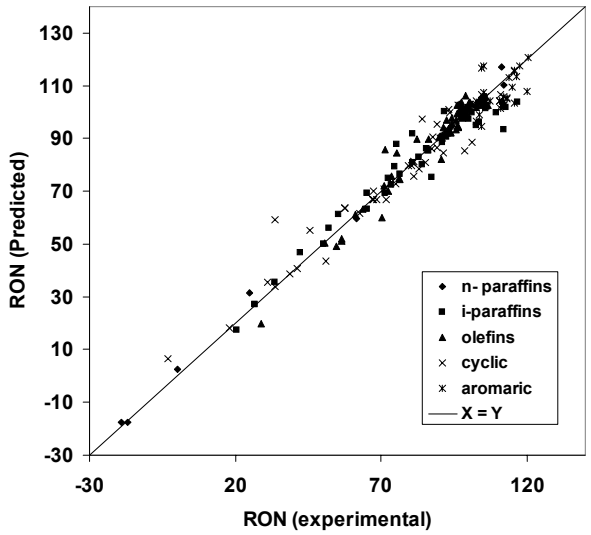

Figure 1. Parity plot for the RON of 200 pure hydrocarbons using structural group contributions.

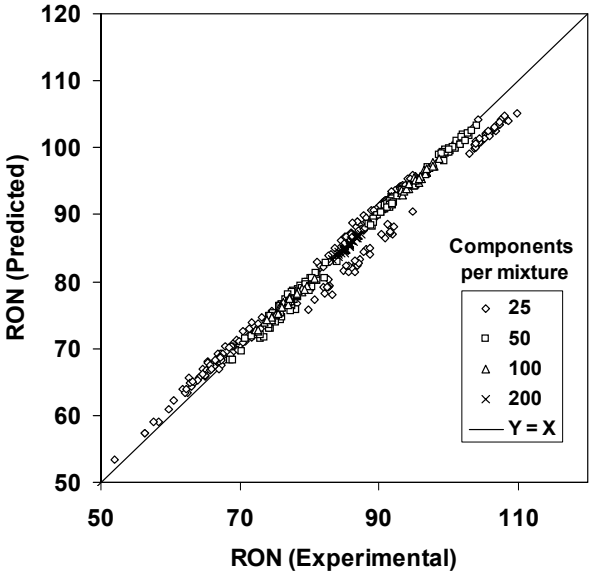

Figure 2. Parity plot for the RON of 560 hydrocarbon mixtures using structural group contributions.

Discussion

Even though the average deviation in the predicted octane numbers for pure components was 4 and the maximum deviation was 26. As expected, when the same were applied to multicomponent mixtures, the over and under estimation in the predicted octane numbers of the individual components cancelled with each other. This effect is very clear for mixtures of 50 or more components. For mixtures of 100 or more components the confidence level is very high (Table 2) and the predicted octane numbers are very accurate. For mixtures of 200 components, the average and maximum deviations were as low as 0.25 and the 0.7 octane number, respectively.

The model appears to be dependent only on the structure of the molecules. Our efforts to include correlating functions using the pure components physical properties either in the group contributions themselves ($\sum$(ON)i) or Equation (1) did not provide any improvement in the predictions. This is probably because these properties are already incorporated in the structural groups themselves.

In conclusion, an estimation technique of octane rating of pure hydrocarbons, though essential, is inexistent. The group contribution approach presented here is the first and proves to be a powerful tool for predicting the octane number of pure hydrocarbons and multicomponent mixtures if coupled with an estimation technique for composition. This method is useful for the automatic generation and reliable estimation of octane number of pure components, for which no data exists, with the objective of estimating octane number of motor gasoline. The clear advantage of the method is its ability to estimate accurately enough the knock rating of a hydrocarbon if the chemical structure only is known.

Acknowledgment. This work was supported by Kuwait University, Research Grant No. EC04/01.

References

1. Baird, C.T.; "Crude Oil Yields and Product Properties", Ch. De la Haute-Belotte 6, 1222 Vezenaz, Geneva, Switzerland, **1981**.
2. Neurock, M; Nigam, A.; Trauth, D.; Klein, M.T, Chemical Engineering Science, **1994**, 49(24A), 4153-4177.
3. Reid, R.C.; Prausnitz, J.M.; Polling B.E.; The properties of gases and liquids, Hill: N.Y., **1987**.
4. The American Petroleum Institute, API Technical Data Book on Petroleum Refinin', **1986**.

Studies on Adsorption and Dissociation of Methane and Carbon Dioxide on Nickel Catalyst

*Ling Qian, Zi-Feng Yan**

Division of Fuel Chemistry
State Key Laboratory for Heavy Oil Processing
University of Petroleum
Dongying, China 257061

Introduction

During the past decades, the process of carbon dioxide reforming with methane has received attention, and efforts have focused on development of catalysts which show high activity towards synthesis gas formation, and are also resistant to carbon formation, thus displaying stable long-term operation[1]. One reason for this renewed interest is of environmental considerations since the reaction consumes carbon dioxide and methane, which are the serious well-known greenhouse gases. Another factor leading to the increased interest in the process is that this reaction offers a suitable H_2/CO ratio needed in F-T synthesis. The key to this process is to develop the optimum catalysts. Numerous materials have been tested as potential catalysts for carbon dioxide reforming with methane, while supported noble metal catalysts as well as Ni-based catalysts have been found to exhibit promising catalytic performance[2-3]. However, the major obstacle encountered in this process is rapid catalyst deactivation by carbon deposition on nickel catalyst surface.

Carbon deposition over catalysts is the fatal problem for carbon dioxide reforming with methane. Although some noble metals show high activity and selectivity for carbon-free operation, high cost and limited availability of noble metals prevent the commercial use of this reaction. It is, therefore, more practical to develop an improved nickel-based catalyst which exhibits stable operation for a long period of time.

Carbon dioxide reforming with methane are particularly important reactions took place on a metal surface. Despite their potential usefulness in energy industry and environment optimization, the nature of the active carbonaceous species produced by the dissociative adsorption of methane and/or carbon dioxide and the detailed mechanism of the reforming reactions are not yet known. It is rather important to clarify the stability, reactivity, selectivity and other properties of the carbonaceous species adsorbed on a metal surface.

Experimental

Catalyst Preparation. The supported nickel catalysts were prepared by a conventionally incipient wetness impregnation method, with aqueous solutions of nitrates as promoter and metal precursors[4]

Catalyst Characterization. The catalyst sample (100mg) was firstly pretreated in an O_2 flow of 20ml/min at 973K for 30min, then the O_2 flow was switched to a H_2 flow of 30ml/min and reduced for 1hr. After the sample was cooled to room temperature in H_2 flow, a 30ml/min He flow was introduced to purge the sample for 30min.

TPR, TPD, TPSR and pulse reaction experiments were carried out in an apparatus, which consisted of a flow switching system, a heated reactor, and an analysis system (**Fig. 1**).

Correspondence should be addressed. E-mail: zfyancat@hdpu.edu.cn
zfyan@hdpu.edu.cn

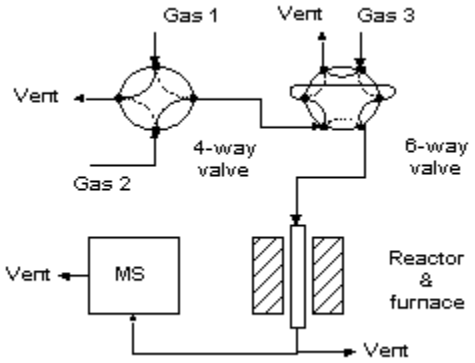

Figure 1. Schematic of the transient response kinetic analysis system

TPSR experiments were also performed in the quartz-fixed-bed micro-reactor. CH_4 was continually pulsed into the catalyst at certain temperature and then the reactor was quickly cooled to room temperature. Subsequently, a 30ml/min flow of H_2/He (1:2) or CO_2/He (1:10) was introduced to flush the reactor continuously to take away the mixture of gases and physically adsorbed. After that treatment, the surface intermediate species produced in the reforming process were well characterized by TPSR in the mixed gas flow. The desorbed species from the metal surface along with the temperature-programmed process were simultaneously detected by the *on-line* DYCOR quadrupole mass spectrometer.

TPD experiments were conducted at a constant heating rate (23K/min), using ultra high purity He as carrier gas, at a flow rate of 30ml/min. When the required adsorption temperature reached, the flow was switched to CO or CH_4 flow. The tested gas adsorbed on the sample for 30 min. Then the flow was switched again to flush the reactor after cooling to room temperature in the adsorption gas flow. Next temperature programming was initiated and the analysis of the desorbed gases was performed with an *on-line* quadrupole mass spectrometer (DYCOR Quadrupole, Ametek Instrument). In the TPD process, the helium gas was dried with $Mg(ClO_4)_2$ and deoxygenated with 402 deoxygenating reagent. The residual oxygen in carrier gas that flowed over the catalyst was removed by cold trap of liquid nitrogen before flowing into the reactor. Leak tests on the reaction system were also strictly performed to exclude the possibility of the oxidation of surface carbon.

XPS for nickel samples was conducted on a VG ESCALAB 210 X-ray photoelectron spectrometer with Mg Kα radiation and a base pressure of 10^{-8}Pa. The specially designed pretreatment cell made sure that the transfer of the XPS sample was not exposed to air before XPS experiments. The Si_{2p} level, with a binding energy of 102.7eV, was used to correct the charge effect as the reference line. The Fisons Eclipse Data System was used to perform the data acquisition and analysis.

The pulse reaction experiments were conducted in the quartz fixed-bed reactor following the catalysts pretreatment. Methane was pulsed continually on the pretreated catalysts using high purity helium as carrier gas at 973K. Subsequently, a 20ml/min flow of H_2/He (1:2) or CO_2/He (1:10) mixture was introduced to flush the reactor continuously to take away the gaseous and physically adsorbed mixture. Then TPSR was initiated in the flow of H_2/He (1:2) or CO_2/He (1:10) at a heating rate of 23K/min. When the temperature was increased to 973K, the carrier gas was switched again, then 0.39ml of H_2, CO_2, or O_2 were continually pulsed respectively into the micro-reactor under high temperature. The desorbed products from the metal surface were simultaneously detected by the *on-line* DYCOR quadrupole mass spectrometer.

Results and Discussion

Methane decomposition on transition metal surface is a thermally assisted catalytic activated process. The reactive sticking of alkanes on nickel single crystal surfaces is strongly dependent on the surface structure. For example, methane reactivity is seen to increase in the order of Ni (111) < Ni (110) < Ni (100) with prolonged exposure to methane[5]. Initial reaction rates for Ni (110) and Ni (100) surfaces are rather similar, and are 7~10 times greater than the initial rate for the Ni (111) surface at 450K. In this study, several questions are addressed. Firstly, how do carbonaceous fragments, in particular the simplest fragment-$CH_{x(ad)}$ species, bond to metal surfaces with more complex structure than that to single crystal surfaces? Secondly, low-index nickel single crystal surface should be effective toward the decomposition of methane, but can alumina-supported nickel catalyst surface be effective in the decomposition of methane? What is the mechanism of thermal decomposition of methane on alumina-supported nickel catalysts? TPSR, TPD, XPS techniques are used to identify surface-bound species and gas-phase products of decomposition of methane adsorbed on alumina-supported nickel catalysts.

For the reaction of CO_2 reforming with methane, the most probable slow steps are methane activation to $CH_{x(ad)}$ (x = 0 ~ 3) species, and the reaction between $CH_{x(ad)}$ species and the oxidant, either in the form of oxygen adatoms originated from CO_2 dissociation or CO_2 itself. Experiments have confirmed that methane promotes the dissociation of carbon dioxide on the catalysts. The promotion of carbon dioxide is attributed to the effect of hydrogen formed in the decomposition of methane. It seems that the key to elucidation the nature of the CO_2 reforming with methane over Ni/γ-Al_2O_3 catalyst is to reveal mechanistic scheme of activation and dissociation of methane.

A great effort was made to detect adsorbed carbonaceous $CH_{x(ad)}$ fragments formed in the decomposition of methane by means of sensitive *in-situ* FT-IR spectroscopy. However, no adsorption bands attributable to any vibration modes of carbonaceous $CH_{x(ad)}$ species were identified either by *in-situ* measurements or after a sudden cooling of the sample in a continuous methane flow at 700K. This means that carbonaceous $CH_{x(ad)}$ species react or decompose too quickly at high temperature, or their surface concentrations are below the detection limit.

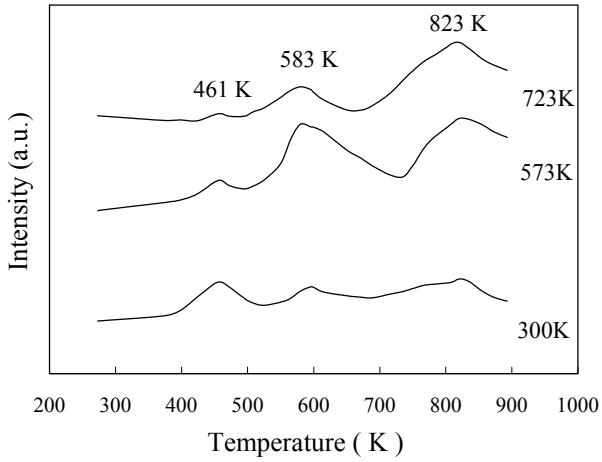

Figure 2. TPSR spectra of CH_4 in H_2 flow on fresh 8wt% Ni/Al_2O_3 at different adsorption temperatures

However, the presence of surface carbonaceous $CH_{x(ad)}$ species was well manifested by its reaction with hydrogen. After flushing the reactor with H_2/He (1:2) flow (following methane decomposition at a certain temperature), the hydrogenation of the surface carbonaceous $CH_{x(ad)}$ species was investigated by TPSR technique. **Figure 2** showed that the decomposition of methane could result in the formation of at least three kinds of surface carbon species on supported nickel catalyst. Generally, the carbon deposition is comprised of various forms of carbons, which are different in terms of reactivity. The distribution and features of these carbonaceous species depend sensitively on the nature of transition metals and the conditions of methane adsorption. These carbonaceous species can be described as: completely dehydrogenated carbidic C_α type, partially dehydrogenated CH_x ($1 \le x \le 3$) species, namely C_β type, and carbidic clusters C_γ type formed by the agglomeration and conversion of C_α and C_β species under certain conditions. A fraction of the surface carbon species, which might be assigned to carbidic C_α (~461K), was mainly hydrogenated to methane even below 500K. It showed that carbidic C_α species is rather active and thermally unstable on nickel surface. The carbidic C_α species was suggested to be responsible for CO formation[6]. The significant amount of surface carbon species was hydrogenated to methane below 600K and was assigned to partially dehydrogenated C_β (~583K) species. The majority of the surface carbon was hydrogenated above 800K and was attributed to carbidic clusters C_γ (~823K)[6].

It also indicated that the formation of three kinds of surface carbon species with different structures and properties largely depend on the exposure temperature and duration to methane. When the nickel catalyst was exposed to methane above 723K, the carbidic C_α species was not detected, and a significant amount of C_β was transformed into the carbidic clusters C_γ. It showed that the carbidic clusters C_γ species might be the precursor of the surface carbon deposition, which may be produced by the interactions between C_α and C_β species and between C_α and C_β themselves.

Figure 3 showed CO_2 TPD on fresh 8wt% Ni/Al_2O_3 catalyst after pretreatment. CO_2 was adsorbed on the catalyst at room temperature (300K). A broad CO_2 desorption peak appeared at 420K on the CO_2 TPD profiles and CO desorption was not detected. This exhibited that CO_2 weakly adsorbed on the catalyst and only a kind of adsorption state of CO_2 formed. From the point of thermodynamic view, dissociated adsorption of CO_2 is impossible on the reduced nickel catalyst. Hereby, it was reasonable that no CO_2 dissociation was observed from TPD profiles.

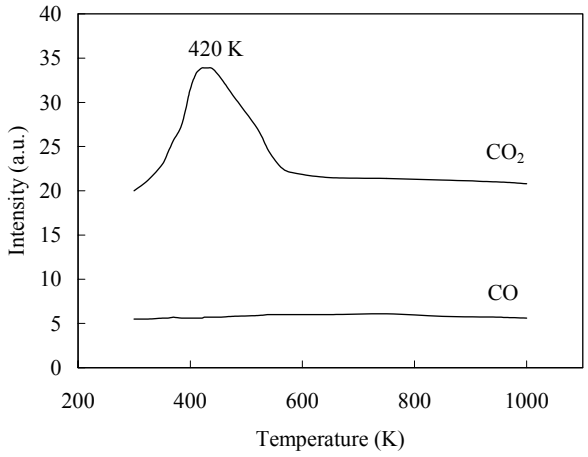

Figure 3. CO_2 TPD over fresh 8wt% Ni/Al_2O_3 catalyst

The CO TPD profiles over the fresh Ni/Al_2O_3 catalyst were

obtained following CO adsorption at 300K (**Figure 4**). The response of CO_2 formation was recorded to monitor the occurrence of CO disproportionation during the process of temperature programming. It was observed that two apparent CO_2 desorption peaks appeared at 410K and 570K, but the intensity of CO remained almost unchanged. The CO_2 desorption peak at 410 K was similar to the CO_2 peak on the CO_2 TPD profiles, which desorbed at 420K. It indicated that CO disproportionation reaction occurred at room temperature and weakly adsorbed CO_2 was formed. The CO_2 desorption at 570K may be derived from disproportionation of strongly adsorbed CO on the catalyst.

As shown in **Figure 5**, TPD spectra of methane on fresh Ni/Al_2O_3 catalyst exhibited that three corespondent peaks of CO_2 were observed. It means that methane decomposition on transition metals truly takes place and the reactivity of the surface carbon species depends sensitively on the varieties of the reactions.

For TPSR spectra in the flow of hydrogen, desorbed product is mainly methane (Figure 2). But for TPD spectra in the flow of helium, desorbed species were mainly CO_2 and some CO, which means that the TPD process was actually a process of temperature-programmed oxidation (TPO), in which the surface carbon was oxidized to form CO and CO_2. The surface oxygen species, which resulted in the oxidation of surface carbon, might be the residual or remaining surface bonded oxygen (M-O) on transition metals. The oxygen atoms in subsurface and bulk phase of the metal cannot migrate to the surface below 1000K[7].

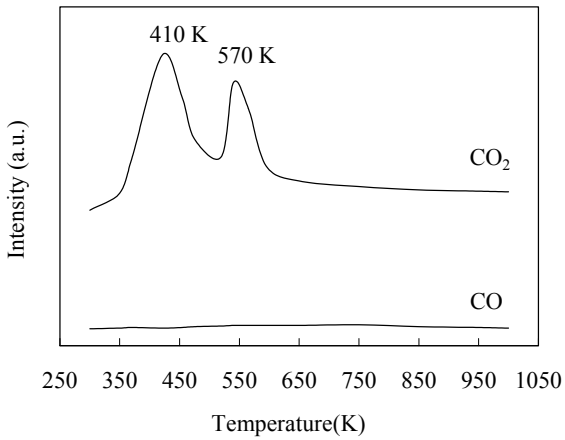

Figure 4. CO TPD over fresh 8wt% Ni/Al_2O_3 catalyst.

Furthermore, XPS results showed that the crystalline oxygen of alumina support does not interact with the surface carbon at moderate temperature (< 850K). Thus, the CO and CO_2 produced during TPD process might originate from the partially reduced oxygen bonded to metal. This kind of bonded oxygen is rather difficult to be reduced under the pretreatment conditions and cannot migrate from one site to another. It also means that the residual NiO_x species dispersed on the surface of supported nickel catalyst were stepwise reduced during the reaction.

During the TPD process, the surface carbon produced by the decomposition of methane might migrate to the sites of bonded oxygen and interact with them to form carbon oxides. It means that peak temperature gaps (ΔT) of correspondent surface carbon species between TPD and TPSR might be the parameters of characterizing the mobility of the different surface carbon (Figure 2 and 5). An examination of the peak temperature gap indicated that the mobility of different surface carbon species on nickel catalyst is consistent with the order of $C_\gamma > C_\alpha > C_\beta$, with the ΔT value of 0, 5, and 34K, respectively. This indicated that the carbonaceous species formed by the decomposition of methane are mobile enough and interact with partial metal oxide to form CO_2. In the meantime, from Figure 5 another conclusion can be drawn that C_α and C_β species could be transformed into C_γ species and the transformation could be accelerated with the increasing adsorption temperature, similar to those exhibited in TPSR studies (**Figure 2**).

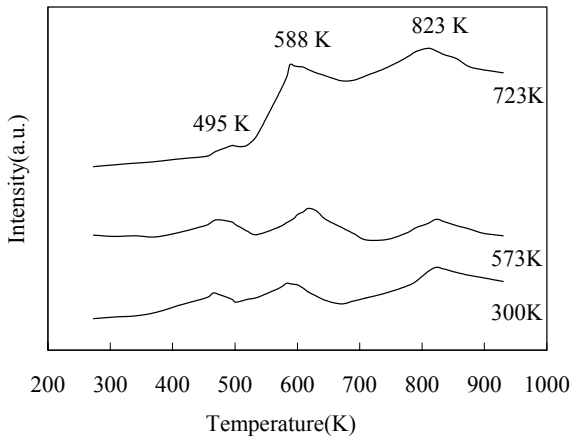

Figure 5. TPD spectra of CH_4 in He flow on fresh 8wt%Ni/Al_2O_3 catalyst at different adsorption temperatures.

The TPD profiles of used Ni/Al_2O_3 catalyst after 4hrs of reforming reaction were shown in **Figure 6**. The response of CO_2 formation was recorded to monitor the occurrence of CO disproportionation during the process of temperature programming. Compared with CO-TPD profiles over the fresh Ni/Al_2O_3 catalyst, on which two respective CO_2 desorption peaks appeared, the TPD profiles on used catalyst were different. An additional intense CO_2 peak at ca. 910K was observed on used catalyst. The CO desorption was also increased with increasing temperature from at ca. 810K.

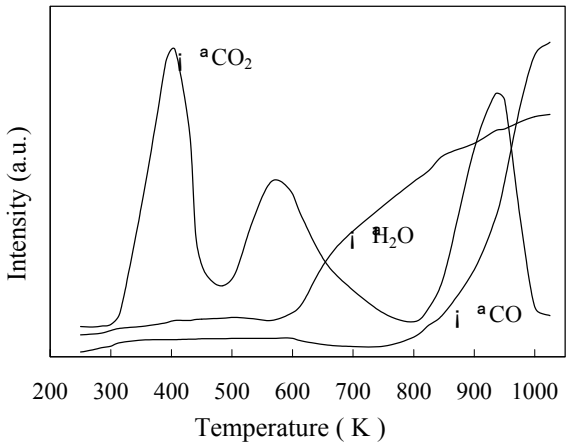

Figure 6. TPD profiles over used 8wt% Ni/Al_2O_3 catalyst after 4hrs of reforming reaction.

The two CO_2 desorption peaks appeared on both CO-TPD profiles over the fresh and used catalysts at ca. 410K and 570K. They seemed to correspond to the desorbed CO_2 in the form of weak chemisorption on different sites on both catalysts. It was interesting to note that a large quantity of CO and CO_2 desorbed at approximately the same temperature from at ca. 800K, but the

increase of CO obviously lagged behind. This could be manifested by the mobility of the surface carbon species and the reactivity of the oxygen species on the nickel catalyst. The mobile surface carbon species can attack the neighboring oxygen adatoms or surface oxygen species to form CO_2. It was also possible that the CO_2 desorbed from the catalyst re-adsorbed and then reacted with surface carbonaceous species to produce CO. The obvious hysteresis effect of CO peak with respect to CO_2 indicated that CO might be the secondary product rather than primary one.

The XPS experiments and Ar^+ etching techniques could give more supporting information. The binding energy data of the catalyst calcined in air at 973K, reduced in H_2 at 973K and exposed to methane followed by reduction were submitted by XPS experiments. The results showed that surface nickel exists in oxidative state (B.E. 856.00eV) for calcined sample, partially oxidative state (B.E. 853.64eV) for reduced sample in H_2 and metallic state (B.E. 852.90eV) for methane exposed sample (Figure 7). The binding energy of metal Ni is 852.30eV, so it is derived that the catalyst exposed to methane following reduction exists essentially in metallic state. This is also consistent with the CH_4 TPD results above (Figure 5). That is to say, the residual NiO_x species dispersed on the surface of supported nickel catalyst can be stepwise reduced during the reaction.

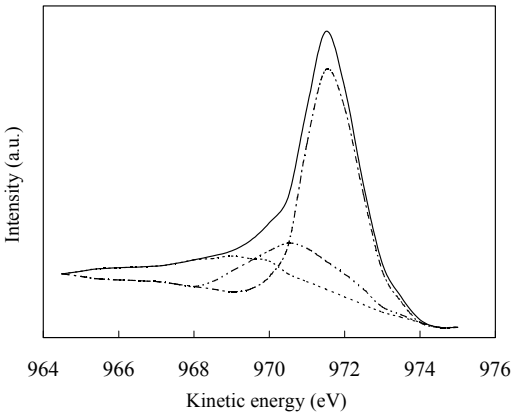

Figure 7. Deconvoluted XPS of C(1s) of 673K-adsorbed CH_4 at 300K.

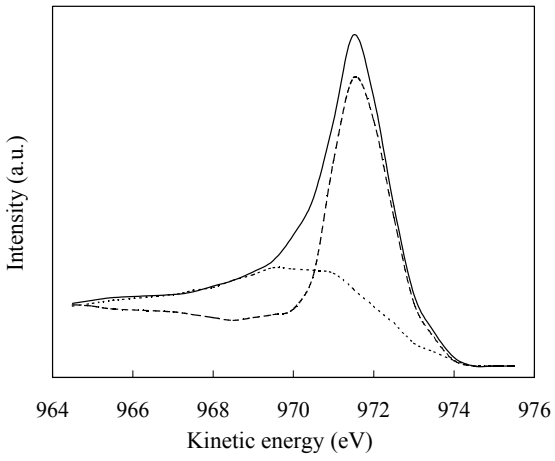

Figure 8. Deconvoluted XPS of C(1s) of 673K-adsorbed CH_4 after sputtered by Ar^+ ions of 1.36×10^{-4}Pa at 300K and 5kV for 5min.

Figure 7 showed that methane decomposition on supported nickel catalyst can result in three different types of surface carbon, similar to the TPSR results, whose binding energy are 282.00, 282.90 and 284.70eV, respectively. The deconvoluted XPS spectra of C(1s) of 673K-adsorbed CH_4 after sputtered by Ar^+ at 300K were shown in **Figure 8**. Comparison of deconvoluted XPS spectra before and after Ar^+ etching exhibited that C_α (B.E. 282.00eV) and C_β (B.E. 282.90eV) species are thermally unstable and can be transformed into C_γ species (B.E. 284.70eV) under the experimental conditions.

As shown in **Figure 9**, CO_2 TPSR was firstly performed in the mixed gas of CO_2/He (1:10) following CH_4 pulses over reduced Ni/Al_2O_3 catalyst, then the H_2 or O_2 pulse was introduced into the reactor (**Figure 10**). In the same way, H_2 TPSR was performed in the mixed gas of H_2/He (1:2) flow following CH_4 pulses over reduced Ni/Al_2O_3 catalyst, then the CO_2 or O_2 pulse was introduced into the reactor (**Figure 11**).

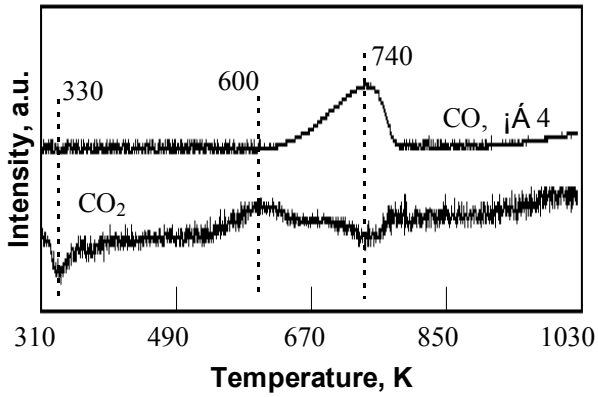

Figure 9. TPSR in CO_2/He (1:10) stream following CH_4 pulses at 973K over reduced Ni/Al_2O_3 catalyst.

A fraction of CO_2 adsorbed on the catalyst at about 300K and desorbed from 600K in the CO_2/He flow. The equilibrium between the surfaced adsorbed CO_2 and gaseous CO_2 was responsible for the high CO_2 desorption temperature than that in He flow (420K). The formation and desorption of CO can be observed while surfaced CO_2 began to desorb greatly. The consumption of CO_2 and formation of CO reached the maximum at increased temperature of 740K. CO_2 TPSR on the Ni catalyst may give a deduction of the reaction pathway of CO_2: firstly adsorbed on the surface of the catalyst, then reacted with neighboring surface carbonaceous species to form CO. This was similar to the inference from the TPD experiment of the used catalyst as **Figure 5** showed.

The formation of CH_4 was not detected in the H_2 pulse reaction following CO_2 TPSR at 973K. It showed that the surface carbonaceous species, which can react with CO_2 feed, had used up. The formation of CO was not detected in the CO_2 pulse reaction following H_2 TPSR at 973 K, either. It showed that the surface carbonaceous species which can react with H_2 had used up. This type of surface carbonaceous species was active and can react with not only CO_2 but also with H_2. At the same time, other inertial carbonaceous species may exist on the surface of the catalyst. The O_2 pulse reaction was continually carried out following the H_2 or CO_2 pulse reaction in order to verify the existence of other carbonaceous species. The appearance of CO_2 pulses was good evidence for the existence of the other carbonaceous species, which was difficult to react with H_2 or CO_2. The catalyst deactivation may result from the deposited carbon species which only reacts with O_2 even at very high temperature.

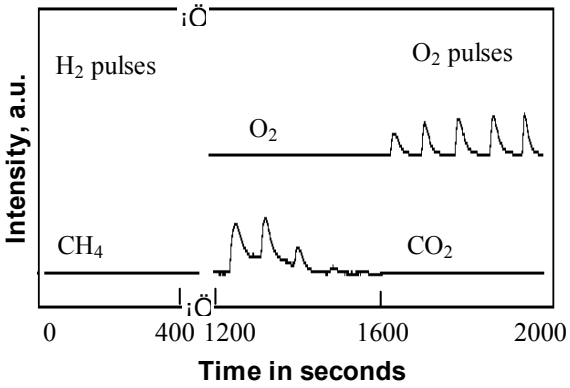

Figure 10. H_2 and O_2 pulses patterns at 973K following CO_2 TPSR over Ni/Al_2O_3 catalyst.

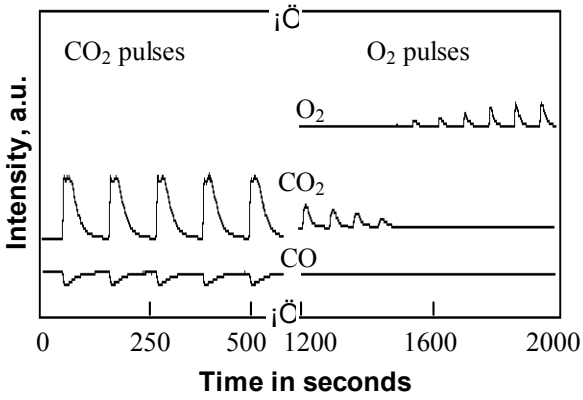

Figure 11. CO_2 and O_2 pulse patterns at 973K after H_2 TPSR over Ni/Al_2O_3 catalyst.

Figure 2 became conscious of the emergence of at least three kinds surface carbonaceous species produced by the decomposition of methane at lower temperature. When the catalyst was exposed to methane at 973K, the carbidic C_α species was completely converted into C_β or C_γ species. The partially dehydrogenated C_β species can react with H_2 or CO_2 to form CH_4 or CO, but the less active carbidic clusters C_γ species can not react with H_2 or CO_2, but react with O_2 at high temperature. The H_2 and CO_2 TPSR and pulse reaction provide the mutual verification of the existence and property of the surface carbonaceous species.

Based on all the above studies, the possible reaction processes of carbon dioxide reforming with methane can be inferred as follows: methane is firstly decomposed into hydrogen and different surface carbon species, then the absorbed CO_2 reacts with surface carbons to form CO. The pattern of activation and reaction of methane with carbon dioxide on the supported nickel catalysts is shown as **Figure 12**.

Conclusions

TPSR and TPD showed that the decomposition of methane results in the formation of at least three kinds of surface carbon species on supported nickel catalyst and that the distribution and features of these carbonaceous species depend sensitively on the nature of transition metals and the conditions of methane adsorption.

Carbidic C_α, carbonaceous C_β and carbidic clusters C_γ surface carbon species formed by decomposition of methane showed different surface mobility, thermal stability and reactivity. C_α and C_β species on the nickel surface are thermally unstable and can be rapidly converted into C_γ species upon the increasing temperature. The carbidic carbon is a very active and important intermediate in the carbon dioxide reforming with methane and the carbidic clusters C_γ species might be the precursor of the surface carbon deposition.

CO_2 TPD exhibited that CO_2 weakly adsorbs on the catalyst and only a kind of adsorption state of CO_2 formed. CO TPD indicated two kinds of adsorption states of CO exist on the catalyst and desorbed in the form of CO_2 at different temperatures by the CO disproportionation reaction.

The CH_4 TPD process actually undergoes a TPO process involving the surface residual oxygen species on reduced nickel catalyst. CO and CO_2 produced during TPD process might originate from the partially reduced residual oxygen bonded to metal. It can be used to evaluate the mobility of the surface carbon species.

The partially dehydrogenated C_β species can react with H_2 or CO_2 to form CH_4 or CO, but the less active carbidic clusters C_γ species can not react with H_2 or CO_2, but react with O_2 at high temperature. The catalyst deactivation may result from the deposited carbon species which only reacts with O_2 even at very high temperature.

The possible interaction mechanism of carbon dioxide reforming with methane is that methane is firstly decomposed into hydrogen and different surface carbon species, then the absorbed CO_2 reacts with surface carbons to form CO.

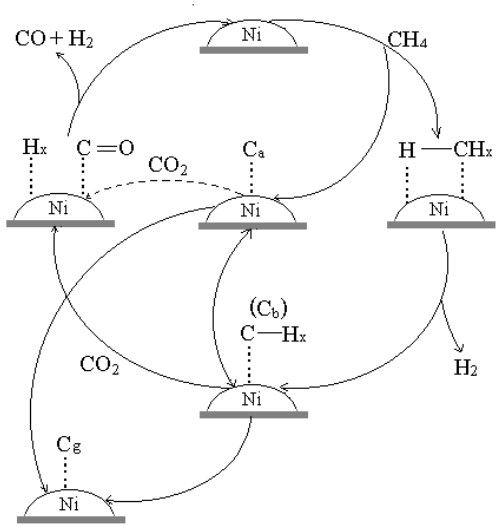

Figure 12. Patterns of activation and reaction of CH_4 with CO_2 on the nickel catalyst (C_a represents carbidic species – C_α, C_b represents carbonaceous species – C_β, C_g represents carbidic clusters species – C_γ. The dotted line represents less possible pathway.)

References

(1) Fischer, V. F.; Tropsch, H. *Brennst. Chem.,* **1928**, *3*(9), 39.
(2) Ding, R.-G.; Yan, Z.-F.; Qian, L. *Natural Gas Chemical Industry (Tianranqi Huagong)*, **1999**, *24*, 50.
(3) Rostrup-Nielsen, J. R.; Hansen, J. H. B. *J. Catal.,* **1993**, *144*, 38.
(4) Yan, Z.-F.; Ding, R.-G.; Song, L.-H.; Qian, L. *Energy & Fuels*, 1998, *12*, 1114.
(5) Beebe, T.P.; Goodman, D.W.; Kay, B.D.; Yates, J.T. *J. Chem. Phys*., **1988**, *92*, 5213.
(6) Zhang, Z.; Verykois, X. E. *Catal. Today,* **1994,** *21*, 589.
(7) Yan, Z.-F.; Xue, J.-Z.; Shen, S.-K. *J. Natural Gas Chem*., **1996**, *5*, 51.

STUDY ON MOLECULAR INTERACTIONS IN PETROLEUM RESIDUE BY ULTRA-VIOLET SPECTROMETRY

Aijun Guo, Zongxian Wang, Bin Shi, and Guohe Que

National Laboratory of Heavy Oil Processing, University of Petroleum, Dongying 257061, P.R. China

Introduction

Heavy petroleum is a valuable energy resource now and may even be a priceless material for non-fuels such as polymers in the future. However most probably, it has to be upgraded into light liquid fuels or small building units of polymers before taking advantage of it. In the upgrading process, molecular interactions are important for operation efficiency and product distribution.

Residue is a major form of heavy petroleum. Much research work has been devoted to molecular physical interactions in residue. Most work leads to the concept that in upgrading process, association between asphaltene molecules is the dominant factor controlling coke formation when evaluating the associations among saturate, aromatic, resin, and (or) asphaltene molecules. It sounds reasonable because an asphaltene molecule is most likely to include aromatic ring sheet of highest aromaticity, to have highest content of heteroatoms, and to have highest molecular weight. However just as James Speight predicted that since the physical properties of asphaltenes were measured after its separation out of petroleum system, the actual state of *in-situ* asphaltene molecules might be quite different from what the collected data presented [1].

This research aims to investigate the molecular physical interactions of different petroleum residua, and then to postulate a modified model on residue's physical structure.

Experimental

Sample. Selected properties of Liaohe vacuum residue (LHVR) and Gudao vacuum residue (GDVR) and their subfractions are listed in Table 1 and Table 2, respectively.

Isolation of Four Sub-fractions. LHVR and GDVR were firstly precipitated into asphaltenes (asp) and maltene. Then the maltene was chromatographically separated into saturates (sa), aromatics (ar), and resins (re). Briefly, 3g residue was mixed with 3mL of benzene, and then 120mL of pentane were introduced into the mixture. After filtering the insolubles (asp), the asp was refluxed by pentane until the refluxed pentane was colorless. The maltene was then chromatographically separated into sa, ar, and re on an alumina (240g, 100-200 mesh, with 1% H_2O) column (20×1350mm) at 50°C, using the following solvents as the corresponding eluents: n-pentane (300mL), benzene (300mL), and benzene/ethanol (1/1 by volume, 150mL) followed by 150mL of benzene and 150mL ethanol.

Ultimate Analysis and Molecular Weight (MW) Measurement. Carlo Erba 1160 elemental analyzer was used for C, H, N, and a tube oven combustion method (similar to ASTM-D1552) for S. Average molecular weight was measured by vapor pressure osmometry (VPO) method (benzene as solvent, 45°C) with a Knauer molecular weight analyzer.

Ultraviolet Spectroscopy Analysis. The absorption spectra were taken on a Varian Cary 50 Probe UV-Visible spectrophotometer with a 0.25 mm slit width (0.5 nm band width). All the samples investigated were dissolved in hot toluene at the concentration of 20.0 $mg \cdot L^{-1}$for absorption measurement at room temperature. Blank absorption spectra by toluene were subtracted (figure 2).

Table 1. Selected Properties of Two Vacuum Residua

Property	LHVR	GDVR
Density/ g cm^{-3}(20°C)	1.0013	0.9756
CCR/ wt%	19.0	15.6
MW	990	810
aromaticity	0.26	0.22
Elemental analysis		
C/ wt%	86.11	85.05
H/ wt%	11.05	11.28
H/C (atomic ratio)	1.53	1.58
N/ wt%	1.22	1.07
S/ wt%	0.36	3.12
SARA fractions		
saturates (sa)/ wt%	18.8	22.3
aromatics (ar)/ wt%	26.4	32.1
resins (re)/ wt%	36.9	32.1
n-C_5 asphaltenes (asp)/ wt%	17.9	13.5

Results and Discussion

Conglomeration of Molecules from a Specific Sub-fraction. When MW of residue is measured by VPO method, the underlying principle is that the presence of small amount of non-volatile solute lowers the vapor pressure of the solution. For easier detection of the small lowering of the pressure, the signal is converted to electric resistant difference, so that the resultant voltage difference (G) may be read on an MW analyzer. For LHVR, GDVR, and their respective sub-fractions, plots of concentration C against G/C are given in figure 1 by using a knauer MW analyzer.

From figure 1 it can be noted that the slopes for GDVR, GDsa, GDar, GDre, GDasp are -0.0485, -0.0784, -0.0489, -0.0297, and -0.0069(g/kg) respectively, or -32, -24, -26, -33, and –82 (kmol/kg). The numerical values of the slopes for the corresponding LHVR and

Table 2. Selected Properties of SARA Fractions from the Vacuum Residua in Table 1

Samples *	LHsa	LHar	LHre	LHasp	GDsa	GDar	GDre	GDasp
MW	540	720	1300	5200	550	710	1060	3440
C/ wt%	86.46	87.07	86.57	86.07	86.31	85.55	83.50	81.89
H/ wt%	13.72	11.02	9.63	8.92	14.30	11.32	9.98	8.99
H/C (atomic ratio)	1.89	1.51	1.32	1.23	1.97	1.58	1.42	1.31
aromaticity	0.00	0.27	0.41	0.49	0.00	0.22	0.34	0.42
N/ wt%	0.00	0.84	2.08	2.20	0.00	0.87	1.43	1.50
S/ wt%	0.01	0.56	0.45	0.36	0.03	4.07	3.19	6.58

***** First two capital letters denote the sources (i.e. LH for LHVR and GD for GDVR) from where the subfractions (denoted by the remaining small letters, i.e. sa, ar, re and asp for saturates, aromatics, resins and asphaltenes) were derived.

its sub-fractions are similar. Therefore the slopes interpret that even in solution as dilute as less than 80g/kg, solute molecules from residue tend to conglomerate. The conglomeration weakens as the solution gets more dilute. It can be inferred that in colloidal residue system, the conglomeration of molecules in any specific sub-fraction group may be quite evident.

By using characteristic viscosimetry [2] (dilute solution with toluene as solvent), narrow cuts' (extracts of supercritical fluid chromatography, or SFC, from residue) molecular size is 1.3~1.5nm. The narrow cuts' SARA distribution is mostly saturates and aromatics, with a little resins and no asphaltenes. So it also shows that conglomeration or association occurs between molecules of residue.

Presumably, the driving forces for conglomeration derive from affinity by molecular similarities. For example, each sub-fraction has different MW, aromaticity, and heteroatom content. When molecules in most sub-fraction groups conglomerate, the left-over molecules are "crowded together" and also appear to conglomerate.

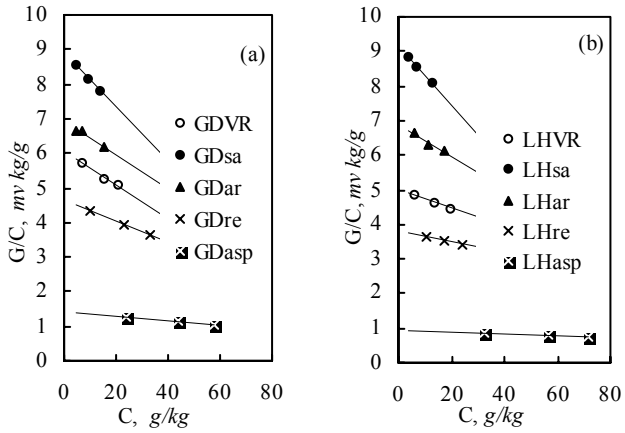

Figure 1. Conglomeration of sub-fractional molecules when measuring MW by VPO method. (a) GDvr and its subfractions; (b) LHvr and its subfractions.

Molecular Association Between Resin and Asphaltene. Structural compositions of the molecules in different sub-fraction group may differ to a large degree. The way of molecular interactions among these molecules therefore must differ from that among molecules of a specific sub-fraction group.

In view of Beer's law, if the multi-component solutes interact, their UV absorptions do not follow law of physical addition. When residue is solved in toluene, by using UV spectrometry, it is possible to investigate intermolecular associations inside residue. In order to facilitate description, association index (AI, table 4) can be defined to be the ratio of Σ (in table 3) to the absorptivity of residue (LHVR or GDVR) at certain wavelength. (1) If AI<1, it means that the association between molecules of the same sub-fraction group (especially resin and asphaltene) is stronger than that between molecules of different sub-fraction groups (especially between resin and asphaltene). (2) If AI>1, it means that the association between molecules of the same sub-fraction group is weaker than that between molecules of different sub-fraction groups. (3) If AI=1, it means that the association between molecules of the same sub-fraction group is as strong as that between molecules of different sub-fraction groups, or the mixture is ideal solution.

Figure 2 is UV absorption spectra of two residua. Based on this figure and similar spectra for all sub-fractions of the residua, absorptivities at selected wavelength are listed in table 3. Table 4 gives a list of AI. According to the AI values, which are greater than 1, association between resin and asphaltene are stronger than that between resins or between asphaltenes. Similar conclusion was reached by using phenol as model molecule on resin [1]. LHVR's AI (1.5) is than that of GDVR (1.1), which shows that association between resin and asphaltene in LHVR is much stronger than that in GDVR. Mix resin and asphaltene by weight ratio of 369:179 for LHVR, or 321:135 for GDVR, and put the mixture in toluene to examine UV absorption. Processed data are tabulated in table 5. Evidently, table 5 is verification for the above conclusion.

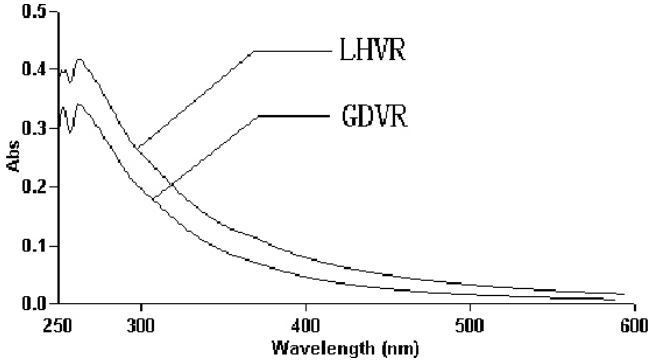

Figure 2. UV absorption spectra of two residua.

Table 3. UV Absorptivity (a) of SARA Subfractions and Residue

	~254*nm*		300*nm*	350*nm*	400*nm*	450*nm*	500*nm*	550*nm*
GDasp	260*nm*	34.530	25.030	15.210	9.145	5.710	3.765	2.585
GDre	259*nm*	27.595	15.695	6.935	3.410	1.800	1.050	0.615
GDar	262*nm*	16.790	6.640	1.820	0.515	0.160	0.055	0.020
GDsa	254*nm*	6.078	0.209	0.100	0.080	0.075	0.070	0.064
Σ	-	20.264	9.945	4.886	2.513	1.414	0.879	0.547
GDVR	262*nm*	17.075	9.835	4.530	2.315	1.295	0.795	0.525
LHasp	261*nm*	37.780	28.410	18.480	12.240	8.260	5.815	4.225
LHre	249*nm*	171.96	31.075	15.455	9.170	5.490	3.345	2.745
LHar	261*nm*	18.565	6.830	2.075	0.670	0.240	0.090	0.04
LHsa	254*nm*	5.518	0.275	0.128	0.110	0.100	0.087	0.080
Σ	-	76.156	18.407	9.583	5.773	3.587	2.315	1.795
LHVR	262*nm*	20.920	12.870	6.760	3.955	2.465	1.635	1.140

a=A/(b·C): a-absorptivity(*L/(g cm*^{3})), A-absorbance, b-light path(*cm*), C-concentration (*g/L*);

Σ: summation of absorptivity in view of SARA percentage composition.

Table 4. Association Index(AI) between Resin and Asphaltene

WL */nm*	~254	300	350	400	450	500	550
GDVR	1.19	1.01	1.08	1.09	1.09	1.11	1.04
LHVR	3.64	1.43	1.42	1.46	1.46	1.42	1.58

Table 5. Association Index(AI) between Resin and Asphaltene

WL */nm*	~254	300	350	400	450	500	550
GD(re&asp)	1.22	1.07	1.12	1.13	1.13	1.15	1.09
LH(re&asp)	3.87	1.46	1.46	1.49	1.50	1.46	1.49

On the other hand, information on intermolecular association can also be learned from wavelength of the first absorption peak in the longer wavelength range. These wavelengths are included in table 3. For both residua, absorption peaks are at 262nm, and for their sub-fractions, absorption peaks are at 249~262nm. This phenomenon also shows that association occurs between molecules of different sub-fraction groups, which further de-localizes conjugated electrons of chroma-producing group, resulting in absorption red-ward shift.

Association must be determined by molecular structure and its chemical composition. Usually residue is a colloidal system, with the clustered and resin-adsorbed asphaltene as dispersed phase, and the oils (i.e. saturates plus aromatics) as dispersing agent. Intermolecular association exists between asphaltenes, between resins, and between asphaltenes and resins. Forces leading to intermolecular association (and hence residue's colloidal stability) are charge transfer effect, dipolar effect and hydrogen bond effect. These forces are the result of heteroatoms and aromatic ring's π-electron cloud. LHVR, GDVR and their sub-fractions are rich in heteroatom (S, N, O, and metals) content, and are also aromatic (tables 1 and 2). It is noteworthy that associations are weak interactions and are in dynamic and reversible process, and that resin molecule is small while asphaltene molecule is large and "porous". Therefore when resin and asphaltene are put together, association between asphaltenes may break up and new association between resin and asphaltene will be formed automatically. So AI is greater than 1, and absorption shifts red-ward. On the other hand, LHVR and its sub-fractions resin and asphaltene are more aromatic than its GDVR counterparts respectively. Hence AI between resin and asphaltene of LHVR is much greater than that of GDVR. This intimates that aromaticity may play a major part concerning association occurring in residue.

Postulation of a Structural Model of Residue. Based on the above discussions, a structural model of petroleum residue is postulated in figure 3. In addition to the well-known characteristics, such as asphaltene being the core of micelle, further clustering of the asphaltene-resin complex, and the lowering in molecular weight and aromaticity in the direction of radiation from the core, in this model two leading characteristics are emphasized. The first is that the association between resin and asphaltene is prevalent in contrast to that between asphaltenes. The second is that for each sub-fraction, the molecules tend to conglomerate.

Conclusions

By using ultra-violet spectrometry and a routine molecular weight test, phenomenon on molecular interactions are observed and analyzed. It is found that the association between resin and asphaltene is superior to that between asphaltenes. The strength of this kind of association varies with source of residue. On the other hand, as far as residue's four sub-fraction (SARA) composition is concerned, molecules in each sub-fraction tend to conglomerate. Finally a structural model of petroleum residue is postulated, which lays emphases on molecular interactions.

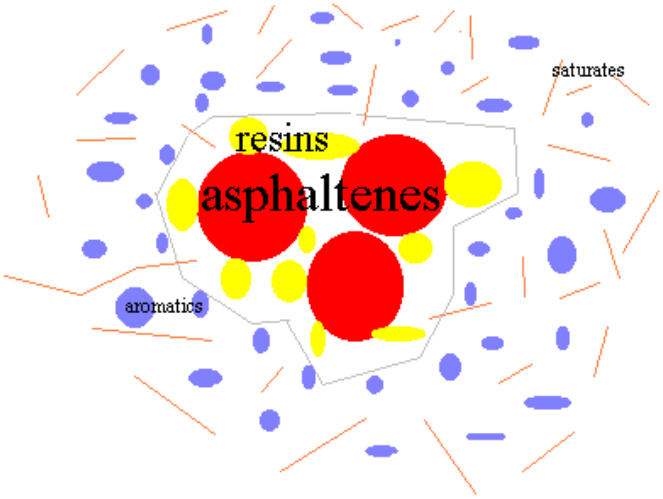

Figure 3. Structural model of residue.

References

(1) Speight, J. G. *The Chemistry and Technology of Petroleum.* Marcel Dekker, Inc: New York, **1991**.
(2) Yang, C. H.; Xu, C. M.; Du, F.; Lin, S. X. *J. Petr*. **1998**, *14(3)*, 34.

THERMAL DECOMPOSITION OF HMX INFLUENCED BY NANO-METAL POWDERS IN HIGH ENERGY FUEL

Shufen Li, Zhi Jiang, Shuqin Yu
Department of Chemistry Physics
University of Science and Technology of China
Hefei 230026, China

Introduction

When the average diameter of particle is less than 100nm, the particle will possess many interesting properties, such as large specific area, little size effect and quantum size effect[1]. Thus, the addition of nano metal powder in propellant will probably be promising for its high reactive ability. The thrust of this work is to investigate the effect of nano metal powder on the decomposition characteristics of cyclic nitramines octahydro-1,3,5,7-tetranitro-1,3,5,7-tetrazocine(HMX)-one of the main energetic ingredients used in various propellants and explosives. Understanding the complex physicochemical process that underlie the combustion of such materials can provide a link between the physical properties and molecular structure of these molecules and their combustive behavior, which in turn, may offer some clues for application of nano metal powder in propellant and explosive to obtain better control of their ignition, combustion or sensitivity.

Experimental

Thermal Analysis. The work of thermal analysis was performed with a Mettler TA910 Pressure Differential Scanning Calorimeter (PDSC) system and a Mettler TA2950 thermogravimetry. Almost constant sample mass of 0.5±0.1mg placed in encapsulated aluminum pans was used in all experiments with the heating rate of 10℃/min. Nitrogen with high purity of 99.99% was used and its flowing rate in the balance and stove of thermogravimetry was 40ml/min and 60ml/min respectively.

Metal powder characterization. JSM-5800 SEM made by JEOL Ltd. and Y-4Φ XRD by Dangdong Ray Ltd was used to characterize the metal powders. The results were shown in **Table 1**. The leader character n- and g- in **Table 1** represent nano and general grade metal respectively.

Table 1. Average Diameter of Metal Powder

n-Al	n-Ni	n-Cu	g-Al	g-Ni	g-Cu
90nm	10nm	90nm	10μm	1.1μm	3μm

Samples preparation. HMX in technical pure was sieved by screen cloth of 120 mesh. The mixtures of metal powders and HMX at weight ratio of 3:2 were prepared by careful mixing of the two components in a 5-cm diameter polished porcelain container with a polished glass rod. Ethanol absolute was used as dispersant.

Results and Discussion

Three peaks of the DSC curve of pure HMX are shown in **Figure 1**. The weak endothermic peak (T_m=185℃) is due to the transformation of HMX from the low temperature phase (β) to the high temperature phase (δ)[2]. The sharp endothermic peak at 281.95℃ corresponds to melting which is followed by a strong exothermic peak. The sharp peak(T=286.86℃) immediately after the melting is due to the self-decomposition of HMX. The DSC curve of HMX/n-Cu (3:2, by mass) also shown in **Figure 1**. The decomposition peak of HMX changes from a sharp peak to a gentle slope one and shifted 15.92℃ forward.

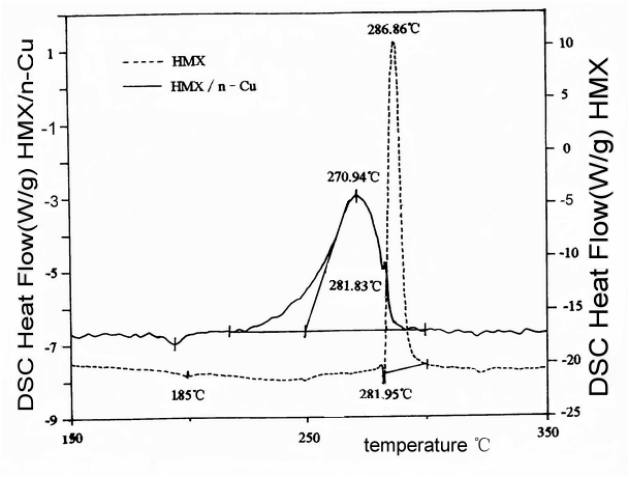

Fig 1 The DSC Curve of HMX and HMX / n-Cu

Table 2 summarizes the data of DSC parameters recorded for the mixture of HMX and metal powder. The results suggest that T_l of HMX remains at 281℃ in all samples and the numerical value of PHC and DTH fluctuated in the same tendency with the different kind of metal. A comparison of PHC among the mixtures of HMX and metal powders shows that n-Cu has the greatest influence on the condensed-phase decomposition of HMX among the nano metal powders. Other nano metal powders grades displayed an intermediate effect while the micron grade powders had the least effect.

Table 2. DSC Result of HMX and Mixture of HMX and Metal Powder(0.1MPa; 10℃/min)

Sample	T_l(℃)	T_O(℃)	T_P(℃)	PHC(%)	DTH(℃)
HMX	281.95	282.48	286.86	1.52	0
HMX/n-Cu	281.83	249.06	270.94	80.7	15.92
HMX/n-Ni	281.09	263.69	283.68	38.5	3.18
HMX/n-Al	281.76	269.04	284.23	35	2.63
HMX/g-Cu	281.48	281.70	284.73	14.7	2.13
HMX/g-Ni	280.43	280.80	284.68	9.14	2.18
HMX/g-Al	281.40	282.14	286.17	2.83	0.69

T_l--liquefied temperature T_O--onset temperature of pyrolysis
T_p--peak temperature of pyrolysis
PHC--percent of heat releasing at condensed-phase decomposition
DTH--difference between T_P of pure HMX and mixtures of HMX and metal

As shown in **Table 3** and **Table 4**, T_p(HMX) will increase and PHC will decrease with the decrease of the content of n-Cu or the increase of the system pressure in HMX/n-Cu. That means the nano-metal effect will be weakened by the decrease of the content of metal powder or the increase of system pressure.

Table 3. DSC Result of HMX/n-Cu with Different Content of n-Cu(0.1MPa; 10℃/min)

Sample HMX/n-Cu	T_O(℃)	T_P(℃)	PHC(%)
1:0	282.48	286.86	1.52
3:2	249.06	270.94	80.7
2:1	263.65	283.70	53.2
3:1	265.54	283.82	41.2
4:1	269.26	285.46	32.4

Table 4. DSC Result of HMX/n-Cu at Different Pressure (3:2, by mass, 10℃/min)

Pressure	Sample	T_O(℃)	T_P(℃)	PHC(%)
0.1MPa	HMX	282.48	286.86	1.52
	HMX / n-Cu	249.06	270.94	80.7
1MPa	HMX	280.37	285.33	0.80
	HMX / n-Cu	277.73	283.01	63.08
5MPa	HMX	277.15	284.60	0.23
	HMX / n-Cu	280.10	282.19	52.5

In the decomposition process of HMX, heating rate is an important parameter in determining what kind of elementary process appears and in what phase the decomposition occurs. As shown in **Figure 2**, the proportion of condensed phase decomposition of HMX in HMX/n-Cu is declined with the increase of heating rate. The appearance of sharp self-decomposition peak of HMX indicates that the controlling step of decomposition of HMX will be the liquid state decomposition process at or above a heating rate of 20℃/min. The software package developed by Mettler TA corp. were adopted to infer the decomposition kinetic properties of HMX/n-Cu from the isothermal DSC results in the temperature range of 260℃ and 265℃. The results illustrated in **Table 5** show that the decrease of the activation energy of the pyrolysis of HMX influenced by n-Cu is 31 KJ/mol. It means that the energy barrier of pyrolysis of HMX will be decreased by n-Cu, and such decline will lead to the pre-pyrolysis of HMX.

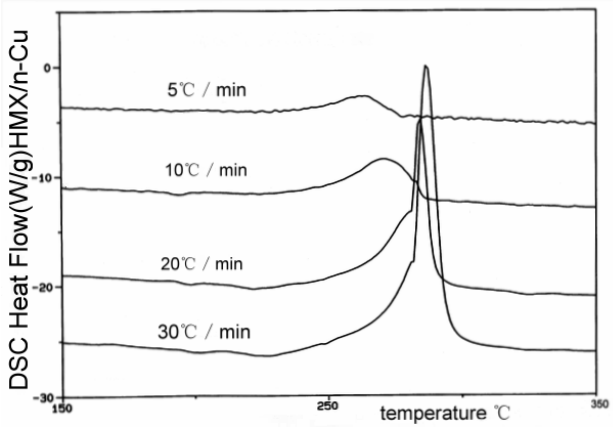

Fig 2 DSC curve of HMX/n-Cu at different heating rate.

Table 5. Kinetic Analysis of the DSC Data over Temperature Range 260 - 265℃

Sample	Activation energy	Log (Frequency factor)
HMX	168 ± 22KJ/mol	15.5 ± 2.1 min^{-1}
HMX/n-Cu	137 ± 16KJ/mol	13.1 ± 1.6min^{-1}

The present work has revealed the definitive influence of n-Cu on the condensed-phase decomposition properties of HMX.

It is well known that copper atoms can react with nitrogen oxide compounds to form complexes and play important catalysis effect in the decomposition of these compounds [3]. The catalysis effect of n-Cu is relative to the unimolecular pyrolysis process of HMX defined as the interaction between n-Cu and the groups of NO_2 in the molecule of HMX.

The secondary effect of n-Cu is defined as the reduction effect of n-Cu on the pyrolysis products of HMX. Product NO is reduced by n-Cu into CuO and N_2. This secondary effect of n-Cu will promote the gas-zone pyrolysis of HMX.

As show in **Table 2**, the existence of nano metal powder such as n-Cu, n-Ni and n-Al will promote the proportion of condensed-state decomposition of HMX. This phenomenon will be attributed to the consequence of more reaction sites—local heat points and physical adsorption sites — offered by nano metal powders. High coefficient of heat conduction of nano metal powder will lead to the formation of local heat points in the heating process of HMX. Once formed, these hot spots will react exothermically to promote the decomposition of the crystal of HMX. More pyrolysis products may be trapped by nano metal powders for more physical adsorption sites formed with the decrease of particle size, such effects will lead to the instability of HMX under heating conditions.

Acknowledgment. We gratefully acknowledge the National Natural Science Foundation of China (NO.59986003) support for this research.

References

1. Ball P., Garwin L., Nature 1992, 355, 761.
2. Kuo K. K., Summerfield M., Fundamental of Solid Propellant Combustion, AIAA. Inc, New York, 1984.
3. Zhou Min F., Andrews L., J. Phys. Chem. A 2000, 104, 2618-2625.